

# Dissertation

## Development of first principles approach on the magnetic anisotropy in Fe/MgO interfaces

## Fe/MgO 界面における磁気異方性に関する第一原理ア プローチの開発

Graduate School of  
Natural Science & Technology  
Kanazawa University

Division of Mathematical and Physical Sciences

Student ID: 1524012014

Name : Nurul Ikhsan

Chief Advisor : Prof. Tatsuki ODA

Date of Submission : 29 June 2018

# Development of first principles approach on the magnetic anisotropy in Fe/MgO interfaces

Nurul Ikhsan

## Abstract

Fe/MgO interface remain attractive for the last decades, and many exciting features make it kernel elements in future spintronics or magnonic devices. However, underlying physical mechanisms of this multi-functional interface remain open to be explored. We performed structural and electronic properties analysis by employing Carr-Parrinello molecular dynamics with fully relativistic Density Functional Theory utilizing planewave basis. Investigation on large perpendicular magnetic anisotropy (PMA) in Cr-buffered Fe/MgO interface from the first-principles approach was performed. The electronic structure shows that the origin of PMA come from the 2-dimensional singularity of the flat band in the  $\bar{X}$ - $\bar{Y}$  line and  $\bar{\Gamma}$ - $\bar{M}$  line, this feature is proposed as the origin of the interface states, which appeared as sharp peak near Fermi level from the density of states. To observe temperature effect to the electronic structure, smearing of Fermi level in the material with the metallic band was proposed. Tuning of the smearing function showed magnetic anisotropy energy (MAE) from spin orbit interaction (SOI) decrease linearly with respect to the temperature, significant change of 0.4 mJ/m<sup>2</sup> observed when the temperature drops from 527K to 10.5K. Changing temperature did the variation of the shape anisotropy, then the SA is included to the total MAE by considering the  $M(T)$  model. These situations introduce competition between MAE(SOI) and shape anisotropy as the temperature increase. Development

on the search for the origin of PMA from the electronic structure and its smearing dependence is our novel approach in first principles calculation of Fe/MgO interfaces.

**Keywords:** *Magnetic anisotropy energy, thickness dependence, temperature dependence, electric field effects, density functional theory, MRAM*

# Contents

<b>1</b>	<b>Introduction</b>	<b>15</b>
1.1	Background and Motivation . . . . .	15
1.2	Development on the perpendicular magnetic anisotropy on Fe/MgO Interface . . . . .	17
1.3	Development on temperature dependence anisotropy . . . . .	19
1.4	Research Objectives . . . . .	20
<b>2</b>	<b>Theory</b>	<b>22</b>
2.1	Khon-Sham . . . . .	22
2.2	Generalized Gradient Approximation . . . . .	23
2.3	Ultrasoft Pseudo Potential . . . . .	24
2.4	Effective Screening Medium . . . . .	26
2.5	Smearing of the Fermi function . . . . .	27
2.6	Magnetic Anisotropy . . . . .	28
2.7	Magnetic Anisotropy Energy . . . . .	29
2.8	MAE from Bruno's relation . . . . .	31
<b>3</b>	<b>Simulation Method</b>	<b>32</b>
3.1	Computational Model of Cr-buffered Fe/MgO . . . . .	33
3.1.1	Integer number of ferromagnetic layer . . . . .	33
3.1.2	Non-integer number of layer(Intermixing in the Fe/Cr interface)	33
3.1.3	Smearing effect of the temperature dependence . . . . .	34
3.2	Computational Parameter . . . . .	35
3.3	Workflow . . . . .	36
<b>4</b>	<b>Result and Discussion</b>	<b>40</b>
4.1	Investigation on large perpendicular magnetic anisotropy energy . . . . .	40

4.1.1	MAE(SOI) . . . . .	40
4.1.2	Fe 2ML case . . . . .	41
4.1.3	Fe 5ML case . . . . .	44
4.1.4	Thickness dependences of interface electronic structure and number of electrons . . . . .	44
4.1.5	Variation of the atomic magnetic moment . . . . .	47
4.1.6	The k-resolved anisotropy . . . . .	48
4.1.7	Total magnetizations . . . . .	49
4.1.8	Shape anisotropy . . . . .	50
4.1.9	Total MAE . . . . .	51
4.1.10	Thickness dependece of electric field effect . . . . .	52
4.1.11	Bruno's relation to the MAE . . . . .	52
4.1.12	The thermal stability of thin layers of ferromagnet . . . . .	53
4.1.13	The origin of oscillating behaviour: Interface states and Quan- tum well . . . . .	54
4.2	Fermi level smearing effect to the MAE . . . . .	56
4.2.1	Magnetic anisotropy from spin-orbit interaction . . . . .	56
4.2.2	Electronic structure . . . . .	56
4.2.3	Including shape magnetic anisotropy . . . . .	58
4.2.4	The change of density of states . . . . .	61
<b>5</b>	<b>Conclusion and Future Works</b>	<b>62</b>
5.1	Conclusion . . . . .	62
5.2	Future Works . . . . .	63
<b>A</b>	<b>Appendix</b>	<b>64</b>
A.1	Thickness dependence of MAE and its EF effect . . . . .	64
A.1.1	Cr(6)/Fe(1)/MgO(5) . . . . .	64
A.1.2	Cr(6)/Fe(2)/MgO(5) . . . . .	67

---

A.1.3	Cr(6)/Fe(3)/MgO(5) . . . . .	69
A.1.4	Cr(6)/Fe(4)/MgO(5) . . . . .	71
A.1.5	Cr(6)/Fe(5)/MgO(5) . . . . .	73
A.1.6	Cr(6)/Fe(6)/MgO(5) . . . . .	75
A.1.7	Cr(6)/Fe(7)/MgO(5) . . . . .	77
A.1.8	Cr(6)/Fe(8)/MgO(5) . . . . .	79
A.1.9	Cr(6)/Fe(9)/MgO(5) . . . . .	81
A.1.10	Cr(6)/Fe(10)/MgO(5) . . . . .	83
A.2	Co Dopping to the Fe(3)/MgO(3) interface . . . . .	85
A.2.1	Type A insertion . . . . .	85
A.2.2	Type B insertion . . . . .	89
A.2.3	Comparative study on Magnetic Anisotropy Energy and Elec- tric Field Effect . . . . .	93
A.3	Different underlayer effect . . . . .	96
A.3.1	W underlayer . . . . .	96
A.4	Magnetic moments of density functional approach . . . . .	98

## List of Figures

1	Schematic model of the slab systems Cr(6ML)/Fe( $x$ ML)/MgO(5ML) for $x = 5$ . . . . .	33
2	Schematic model of the slab systems Cr(6ML)/Fe( $x$ ML)/MgO(5ML) for $x = 3.5$ . . . . .	34
3	Research workflow in generating electronic structure of the target material in Collinear Calculation . . . . .	37
4	Research workflow in generating electronic structure of the target material in Non-collinear Calculation . . . . .	39
5	Thickness dependence of the magnetic anisotropy energy (MAE) from spin-orbit interaction in Cr/Fe( $x$ ML)/MgO. The bullet indicates the experimental value (ref. [50]), where 1ML thickness is assumed to be 0.142 nm. . . . .	40
6	Thickness dependence of the magnetic anisotropy energy (MAE) from spin-orbit interaction in Cr/Fe( $x$ ML)/MgO. In this model we also consider the non-integer layer, where intermixing is possible. The bullet indicates the experimental value (ref. [50]), where 1ML thickness is assumed to be 0.142 nm. . . . .	41
7	Electronic structures at the Fermi level in Cr/Fe(2ML)/MgO without including spin-orbit interaction, (a) projected densities of states (PDOS)(from the top) 3d total $d_{xz+yz}$ , $d_{xy}$ , $d_{x^2-y^2}$ , $d_{3z^2-r^2}$ components, (b) selected $\mathbf{k}$ -point path, and (c) band dispersion for the Fe 3d orbitals at the interface Fe(1) . . . . .	42
8	Electronic structures at the Fermi level in Cr/Fe(5ML)/MgO without including spin-orbit interaction, (a) partial density of states (PDOS), (b) band dispersion for the Fe 3d orbitals at the interface Fe(1) . . . .	44

- 9 Thickness dependence of the number of  $3d$  electron on the interface Fe. The relative values with respect to those of Fe 10ML are shown. The colors of grey, orange (yellow), blue, green, and red are used for total  $3d$  orbital,  $d_{xz+yz}$ ,  $d_{xy}$ ,  $d_{x^2-y^2}$ , and  $d_{3z^2-r^2}$ , respectively. . . . . 45
- 10 Projected density of states (PDOS) for the interface state in Cr/Fe( $x$ ML)/MgO; (a)–(g) for  $x = 1 - 6$  and 9, respectively. The top, middle, bottom lows in the panels show the components of  $d_{xz+yz}$ ,  $d_{xy}$ , and  $d_{x^2-y^2}$ . . . 45
- 11 Atomic magnetic moment of Fe in the ferromagnet layer, Fe(1) are located at the interface of MgO. . . . . 47
- 12 Atomic magnetic moment of Fe in the ferromagnet layer, Cr(1) are located at the interface with Fe. . . . . 47
- 13 The  $\mathbf{k}$ -resolved contribution of MAE: MAE( $\mathbf{k}$ ) for  $x = 2, 3, 4, 5, 6, 9$ , which corresponds from (a) to (f), respectively. The red (blue) color indicates positive (negative) contribution to the MAE from electronic band structure. The non-vanishing typical couplings are described in the right hand side for the positive (negative) area indexed by P (N) in (a)( $x = 2$ ), (d)( $x = 5$ ), and (f)( $x = 9$ ), where the symbol  $o$  (symbol  $u$ ) specifies the states below (above) the Fermi level, and the  $\ell_z$  ( $\ell_x$ ) is the operator of  $z$ -component ( $x$ -component) orbital angular momentum. 48
- 14 Thickness dependence of magnetizations, compared with the available experimental data(ref. [16]). Plus symbol indicates total magnetizations contributed from Fe atom only, solid box includes the contribution of Cr, bullet indicates experimental data. . . . . 50
- 15 Theoretical MAE(MDI) (yellow triangles), normalized MAE(MDI) (blue reverse triangles), and experimental MAE(SA) (red dots), the dashed lines are only guide. . . . . 50

16	Total magnetic anisotropy energy (MAE), compared with the experimental data (bullets)(ref. [16]). The open yellow triangle symbol specifies the data estimated theoretically; MAE(SOI)+MAE(MDI), the reverse blue triangle symbol represent the MAE(SOI+MDI) after the 26% reduction of theoretical atomic moment, and the cross data the sum of the theoretical MAE(SOI) and the shape anisotropy MAE(SA) estimated using the experimental magnetization. . . . .	51
17	The electric field effect change as the thickness of the ferromagnet increase . . . . .	52
18	The estimation from Bruno's relation compared to the calculation of MAE from SOI. Black solid square represent MAE from SOI, red cross symbol are MAE calculated from Bruno relation, blue star symbol are the contribution from Fe(1) at the interface, and orange empty square symbol are contribution from Fe(2). . . . .	53
19	Fermi level smearing effect in magnetic anisotropy energy (MAE) with respect to temperature. The symbols of triangle and circle specify the data by dense and sparse meshes, respectively. . . . .	56

20	<p>(a) Band dispersion curves (left and center) and (b) partial density of states (right) for the minority-spin-state 3d orbital on the interface Fe in the [001] magnetization system determined with the temperature-dependent Fermi level smearings of 316 K (full curves and symbols) and 53 K (broken curves). The symbols specify the angular orbital components projected on the interface Fe atoms; <math>d_{xy}</math>, <math>d_{x^2-y^2}</math>, <math>d_{3z^2-r^2}</math> (left) in blue, green, and red bullets, respectively, and <math>d_{xz}</math>, <math>d_{yz}</math> (center) in orange and yellow. The Fermi levels are adjusted to zero in the vertical axis with the horizontal full line, and the Fermi energy (chemical potential <math>\mu</math>) decreases by 0.11 eV as temperature. The inset figure in (b) shows the typical data of <math>\varepsilon_{n\mathbf{k}} - \mu</math> with respect to the temperature at <math>\mathbf{k} = 0.33 \times \bar{\Gamma}\bar{M}</math> (vertical red arrow). . . . .</p>	57
21	<p>Total magnetic anisotropy energy (<math>K</math>) per unit area with respect to temperature. The symbols of triangle, bullet, circle, diamond indicate the data of <math>T^* = 900, 1100, 1300\text{K}</math> for <math>\Delta K_{\text{sa}}^{\text{int}} = 0</math> and those of cross and plus for <math>T^* = 1300\text{K}</math> and <math>\Delta K_{\text{sa}}^{\text{int}}/A = 0.09\text{mJ/m}^2</math>, where <math>A</math> is the interface area. The empty square symbols specify the experimental data extracted from reference [13]. . . . .</p>	58
22	<p>Temperature dependence on the Density of states of Cr6/Fe5/MgO5 system . . . . .</p>	61
23	<p>The atomic structure model in Cr(6)/Fe(1)/MgO(5) . . . . .</p>	64
24	<p>The density of states of Cr(6)/Fe(1)/MgO(5) . . . . .</p>	65
25	<p>The band dispersion of Cr(6)/Fe(1)/MgO(5) . . . . .</p>	66
26	<p>Electric field effect in Cr(6)/Fe(1)/MgO(5) . . . . .</p>	66
27	<p>The atomic structure model in Cr(6)/Fe(2)/MgO(5) . . . . .</p>	67
28	<p>The density of states of Cr(6)/Fe(2)/MgO(5) . . . . .</p>	67
29	<p>The band dispersion of Cr(6)/Fe(2)/MgO(5) . . . . .</p>	68
30	<p>Electric field effect in Cr(6)/Fe(2)/MgO(5) . . . . .</p>	69

---

31	The atomic structure model in Cr(6)/Fe(3)/MgO(5) . . . . .	69
32	The density of states of Cr(6)/Fe(3)/MgO(5) . . . . .	70
33	The band dispersion of Cr(6)/Fe(3)/MgO(5) . . . . .	70
34	Electric field effect in Cr(6)/Fe(3)/MgO(5) . . . . .	71
35	The atomic structure model in Cr(6)/Fe(4)/MgO(5) . . . . .	71
36	The density of states of Cr(6)/Fe(4)/MgO(5) . . . . .	72
37	The band dispersion of Cr(6)/Fe(4)/MgO(5) . . . . .	72
38	Electric field effect in Cr(6)/Fe(4)/MgO(5) . . . . .	73
39	The atomic structure model in Cr(6)/Fe(5)/MgO(5) . . . . .	73
40	The density of states of Cr(6)/Fe(5)/MgO(5) . . . . .	74
41	The band dispersion of Cr(6)/Fe(5)/MgO(5) . . . . .	74
42	Electric field effect in Cr(6)/Fe(5)/MgO(5) . . . . .	75
43	The atomic structure model in Cr(6)/Fe(6)/MgO(5) . . . . .	75
44	The density of states of Cr(6)/Fe(6)/MgO(5) . . . . .	76
45	The band dispersion of Cr(6)/Fe(6)/MgO(5) . . . . .	76
46	Electric field effect in Cr(6)/Fe(6)/MgO(5) . . . . .	77
47	The atomic structure model in Cr(6)/Fe(7)/MgO(5) . . . . .	77
48	The density of states of Cr(6)/Fe(7)/MgO(5) . . . . .	78
49	The band dispersion of Cr(6)/Fe(7)/MgO(5) . . . . .	78
50	Electric field effect in Cr(6)/Fe(7)/MgO(5) . . . . .	79
51	The atomic structure model in Cr(6)/Fe(8)/MgO(5) . . . . .	79
52	The density of states of Cr(6)/Fe(8)/MgO(5) . . . . .	80
53	The band dispersion of Cr(6)/Fe(8)/MgO(5) . . . . .	80
54	Electric field effect in Cr(6)/Fe(8)/MgO(5) . . . . .	81
55	The atomic structure model in Cr(6)/Fe(9)/MgO(5) . . . . .	81
56	The density of states of Cr(6)/Fe(9)/MgO(5) . . . . .	82
57	The band dispersion of Cr(6)/Fe(9)/MgO(5) . . . . .	82
58	Electric field effect in Cr(6)/Fe(9)/MgO(5) . . . . .	83

---

59	The atomic structure model in Cr(6)/Fe(10)/MgO(5) . . . . .	83
60	The density of states of Cr(6)/Fe(10)/MgO(5) . . . . .	84
61	The band dispersion of Cr(6)/Fe(10)/MgO(5) . . . . .	84
62	The optimized structure of Fe(2)/Fe(1 - x)Co(x)/MgO(3) . . . . .	86
63	The density of states of iron in Fe(2)/Fe(1 - x)Co(x)/MgO(3) . . . . .	87
64	The density of states of cobalt in Fe(2)/Fe(1 - x)Co(x)/MgO(3) . . . . .	88
65	The band dispersion of Fe(2)/Fe(1 - x)Co(x)/MgO(3) . . . . .	89
66	The optimized structure of Fe/Fe(1 - x)Co(x)/Fe/MgO(3) . . . . .	90
67	The density of states of iron in Fe/Fe(1 - x)Co(x)/Fe/MgO(3) . . . . .	91
68	The density of states of cobalt in Fe/Fe(1 - x)Co(x)/Fe/MgO(3) . . . . .	92
69	The band dispersion of Fe/Fe(1 - x)Co(x)/Fe/MgO(3) . . . . .	93
70	The electric field effect of Fe(2)/Fe(1 - x)Co(x)/MgO(3) . . . . .	93
71	The electric field effect of Fe/Fe(1 - x)Co(x)/Fe/MgO(3) . . . . .	94
72	The electric field effect of Fe(3)/MgO(3) . . . . .	94
73	The electric field effect of Fe(5)/MgO(5) . . . . .	95
74	Structure of W(6)/Fe(2)/MgO(5) system . . . . .	96
75	Density of states of the W(6)/Fe(2)/MgO(5) system . . . . .	97
76	Band dispersion of W(6)/Fe(2)/MgO(5) system . . . . .	97

## List of Tables

- 1 Spin magnetic moments in  $\mu_B$  on Cr and Fe atoms. The temperature specifies the value used in the Fermi level smearing. [001]( $z$ -direction) and [100]( $x$ -direction) specify the direction of total magnetization. . . . . 98
- 2 Orbital magnetic moments in  $\mu_B$  on Cr and Fe atoms. The temperature specifies the value used in the Fermi level smearing. . . . . 98

# Acknowledgment

The author wants to personally thanks to Prof. T. Oda for his guidance and encouragement during completing this doctoral thesis. Dr. M. Obata, for all the technical assistance and supportive discussion during this study. Also Prof. M. Saito, Prof. F. Ishii, Prof. H. Nagao, Prof. H. Iwasaki, and Prof. S. Miura for their guidance and valuable feedback during the doctoral research activity in this institution. The author also want to express gratitude for D. Yoshikawa, H. A. Rasyid, I. Pardede, T. Kanagawa, R. R. Septiawan, M. Christivana and also all the computational nano-science lab members for the fruitful discussion in our research period. Also, the author would like to thanks all people in the Department of Mathematical and Physical Science who unmentioned here, who directly related to author during his study.

*Dedicated to my beloved family (Soraya, Aditama, and Megumi) and my parents.*

*For their love, encouragement, and support during the completion of this study.*

*May Allah unite us till Jannah.*

# 1 Introduction

## 1.1 Background and Motivation

The rapid development of computational approach and computing facility are coupling each other accelerating the edge of science. As the third pillar of science, computational could be aid to the experimentalist and theorist or more further as the frontier of science, predicting the undiscovered. Density functional theory (DFT) as the numerical approach to solve the Schrodinger equation has evolved to be powerful tools to understand or predict the physical properties of materials.

In another side, the rapid development of material science and spintronics lead us to the next generation of magnetic technology. This situation has opened the opportunity to advance the technological area such as high-density data storage, ultra-sensitive magnetic sensor, sub-Tera Hertz frequency generator, and magnonic device. Successful development in one of this field may lead to the next industrial revolution.

In this chapter, the author wants to focus the advancement of high-density non-volatile storage. As we know that the third industrial revolution, also known as the digital revolution has brought the computer to become an inseparable part of our life, starting from the personal computer, portable computer, mobile phone, up to important wearable biomedical devices related to one's health. Behind all of this sophisticated devices, there is one crucial component which supports the processor to work, that is the memory. It has been known for decades that there is a pyramid-like architecture of memory implementation in the microcomputer device. This implementation is the best at the current stage, and the memory has its role and requirement depend on how close its location to the processor, the area of the

pyramid slices proportional to the size of memory, the top category in pyramid has the fastest access from the processor. The closer the memory to the processor, it had faster access speed but limited in size. This characteristic is due to the limitation in available space in the fabrication of processor.

This staging strategy is proposed at the early age of the computer, and it is very successful until now. However, there is one caveat, the data movement from the volatile memory to non-volatile memory is energy consuming. Especially for low power and energy efficient device, such as mobile phone, sensor, or internet of things device. Storing data from volatile memory such as SRAM or DRAM to the permanent storage could be energy consuming if there is a significant flow of data in a short period.

The knowledge of material science has open the possibility to create the non-volatile memory which has almost zero power consumption, with more dense capacity, and fast data switching close to current memory use for data register. Discovery of Fe/MgO interface as the recording element of magnetic tunnel junction (MTJ) in the last decade has successfully encouraged the IT industry to fabricate the real non-volatile memory based on this technology.

There are several viewpoints in analyzing requirement for achieving the high-capacity low powered memory. The first consideration is the target of implementation, in which part of the pyramid this memory/storage devices will be implemented. This part will affect to the writing speed requirement, how fast data could be recorded on the MTJ. The primary requirement will be affected with this target such as damping constant.

Next thing to consider is how much power that used to write the device. Naturally, we want to use the lowest possible current (power) to write the memory. This part of energy on the writing technology can be realized by many techniques, starting from spin-polarized current, voltage effect, spin orbit torque, or the combination of it.

Another critical issue is related to error rate and data retention. Direct physical properties related to this requirement is the magnetic anisotropy. The strength of the magnet will define the quality of the data retention and error rate. It will require much energy to modify strong magnet, but the weak magnet would be unstable when exposed to thermal fluctuation or other external disturbance such an artificial magnetic field. Rapid development on the prototype of future memory elements is driving research in the magnetic thin film in both experiment and theoretical area. Substantial need to support future computing machine, motivate us to challenge the current limit in density and power consumption. The primary requirement is to increase the memory density, while maintaining low power consumption.

In summary, the primary target to realize MRAM in a real device are:

- Strong Perpendicular Magnetic Anisotropy (PMA)
- Large Voltage Control of Magnetic Anisotropy (VCMA) [up to 1000 fJ/Vm]
- Low damping constant ( $\alpha$ ) for STT MRAM application
- Low magnetic saturation (Ms)
- Discovery for new writing mechanism/technology (such as Voltage Control  $+\beta$ )

## **1.2 Development on the perpendicular magnetic anisotropy on Fe/MgO Interface**

Fe/MgO interface is the well-known building block of the magnetic tunnel junction (MTJ). Recently this interface becomes prominent candidate for magnetic random access memory (MRAM) application. However, the well establishes MRAM rely on the in-plane magnetized ferromagnet element. The modification of magnet orientation (writing mechanism), still also require induced current. This mechanism also is known as spin-transfer-torque(STT). Recent development on this interface

has successfully achieved the perpendicular magnetization, so that we can optimize the material for high density recording. New writing mechanism also discovered the voltage control magnetic anisotropy (VCMA), or the author prefer to call it the electric field effect (EFE) in this work. It has been one decade since the first finding of tunnel magneto resistance effect in this Fe/MgO. However, we still observe many new physics on this interface.

In the works for the development of the devices, the family of Fe/MgO interfaces has been used as a kernel technological element. They have shown a strong perpendicular magnetic anisotropy for the thin Fe without any heavy element [1, 2]. The multi-functional properties, mentioned in the previous paragraphs, are mostly originated from the electronic structure. In such a system, the interface state has been discussed in the several works [3, 4]. These states are consequences of the band formation consisting of non-bonding orbitals on the interface. Although such character has been observed as new characteristics, detail dependence of electronic structure has not been investigated.

In the recent improvement of computational performance allows us to estimate the magnetic anisotropy or its EF effect precisely and numerically [5, 6]. Such improvement contributes not only to physical and qualitative explanations in the property of magnetic anisotropy but also to semi-quantitative agreements. In particular, the slope in the EF variation has been proved to have a real meaning, when compared with the experimental results [7]. However, in the calculation of magnetic anisotropy energy (MAE), result comparison with experiment still has a gap, to be able to explain the experimental measurements with a quantitative agreement. The experimental progress on the interface magnetic anisotropy in the thin films gives us a fascinating opportunity on a direct comparison between the theoretical and experimental approaches.

This work was devoted to the discussions on electronic, magnetic, and structural properties of Fe( $x$  ML)/MgO(001), as a reinvestigation in the viewpoint of

two-dimensional electronic structure. We obtained remarkable Fe-thickness dependences of MAE, implying a picture of non-rigid band filling in the interface states. Such result can be discussed in terms of electronic band theory, compared with the available experimental data.

### 1.3 Development on temperature dependence anisotropy

Perpendicular magnetic anisotropy (PMA) has an important role for designs of better devices of spin transfer torque recording magnetoresistive random access memory (STT-MRAM) [8, 1]. In the approaches of both theory and experiment, a lot of progress has been made for developing functionals or improving performances [7, 9, 5, 6, 10, 11, 12, 13, 16, 50]. The properties of temperature dependence in PMA are highly requested for designing magnetic materials. Up to now, there are many works of theoretical approach for the systems of localized magnetic moments (single ion-magnetic anisotropies) [18, 19, 20]. In these approaches, the magnetic anisotropy energy ( $K$ ) was treated as a cubic polynomial function of magnetization ( $M$ ). For the metallic epitaxial films, the function of square polynomial were employed at the low temperature [21, 22]. The theoretical approaches showed that  $K$  is proportional to  $M^2$  in case of L1<sub>0</sub>-ordered FePt [23, 24] The recent density functional approach to disordered magnetic bulk alloys explains an anomalous temperature dependence of magnetocrystalline anisotropy [25].

For the design of materials in emerging nanoscale memory and logic device, Alzate *et al.* showed that in the system MgO/CoFeB/Ta-based MTJ [26],  $M$  as temperature dependence fitted well with the Blöch law ( $T^{3/2}$ ) [27]. In addition to this,  $K$  as temperature dependence fitted well with a power law of  $M^2$  or a similar one. Wen *et al.* also showed a similar behavior of temperature dependence on  $M$  and  $K$  in Ru/Co<sub>2</sub>FeAl/MgO-based MTJ [28]. For the thinner films of several iron monolayers, the temperature dependence of  $M$  was implied to change from  $T^{3/2}$  to  $T^2$  [29].

In the materials for perpendicular-MRAM devices, the property of PMA is mainly ascribed to spin-orbit coupling (SOC) in the metallic electronic structure. The magnetocrystalline anisotropy for metal has been estimated successfully since the 1980's using density functional approaches. The PMA of thin films has qualitatively or semi-quantitatively been explained. This is a consequence of the fact that the PMA from SOC overcomes the magnetic shape anisotropy (SA) which favors in-plane magnetization. The latter contribution to magnetic anisotropy has been investigated for a long time, including its temperature-dependent property. However, the temperature dependence of the magnetic anisotropy caused by metallic energy bands has not been investigated very well, particularly for thin film systems.

In the present work, we investigated smearing effects on the Fermi level in terms of the magnetic anisotropy energy of the metal slab system for magnetic devices, by means of a first-principles calculation. These effects are expected to contribute to a temperature dependence on the magnetic anisotropy caused by SOC. In combination with SA analyses, a saturating behavior in  $K$  at room temperatures may be comprehended, compared with the available experimental data [13].

## 1.4 Research Objectives

The purposes of this work are to confirm the mechanism of perpendicular magnetic anisotropy energy and electric field control in Cr buffered Fe/MgO interface by first principles approach. So that we could optimize this interface to enhance its ability in the future. Theoretical understanding of the mechanism on this device holds essential role before we could understand the mechanism, there is a limitation to improve the material properties, but after the findings in the detail of the mechanism, we could clearly define the direction of the improvement.

There is two main objective that highlighted in this research, that is the origin of the perpendicular magnetic anisotropy (PMA) as thickness dependence of the ferromagnet layer, and the temperature dependence of PMA. Our research focus on

---

PMA rather than electric field effect (EFE) because the estimation of PMA is the building blocks of estimation of MAE at each system under a different electric field. However the estimation of EFE also will be presented and discussed in this work. Part of the result of this dissertation is also published in The Science Reports of Kanazawa University [14], [15].

## 2 Theory

### 2.1 Kohn-Sham

Calculation of electronic state are formulated by Kohn-Sham theory. In Kohn-Sham formalism of density functional theory we have to solve the mathematical problem of solving eigenvalue equation:

$$\left\{ -\frac{\hbar^2}{2m} \nabla^2 + V_{ext}(r) + \int \frac{\rho(r')}{|r-r'|} dr' + \mu_{xc}[\rho] \right\} \phi_i(r) = \varepsilon_i \phi_i(r) \quad (2.1)$$

Where the electronic density is given by:

$$\rho(r) = \sum_{i=1}^N f_i |\phi_i(r)|^2 \quad (2.2)$$

In above equation N represent the number of electrons, and  $f_i$  is the occupation number corresponding to one electron eigenstates.

The external potential  $v_{ext}(r)$  represents the interaction between the electron and nuclei, expressed as:

$$V_{ext}(r) = -e^2 \sum_{I=1}^P \frac{Z_I}{|r - R_I|}$$

Finally the last term related to exchange correlation part:

$$\mu_{xc}[\rho](\mathbf{r}) = \frac{\delta E_{xc}}{\delta \rho(\mathbf{r})} \quad (2.3)$$

This equation has to be solved self-consistently as it depends on the solution of Kohn-Sham orbitals equation, shown by Eq. 2.1. And make sure that the density is used to construct the reference potential from Eq. 2.2.

The energy functional of the real system formulated as:

$$E[n(r)] = \int V_{ext}(r) n(r) dr + F[n(r)]$$

where,

$$F[n(r)] = T_s[n(r)] + \frac{1}{2} \iint \frac{n(r) n(r')}{|r - r'|} dr dr' + E_{xc}[n(r)]$$

The exchange correlation part has uncertain value, but we can calculate using some approximation.

We never solve the Kohn-Sham equation analytically for system more than one electron. In most situation we always solve Kohn-Sham equation by numerical approximation or iterative way.

## 2.2 Generalized Gradient Approximation

Based on expression in Kohn-Sham equation, the exchange-correlation energy is a functional of electron spin densities. The density of electron is not always homogeneous, in case of non-homogeneous density, we have to carry out the expansion of electronic density in the term of gradient and higher order derivatives. The exchange-correlation energy can be written as:

$$E_{XC}[\rho] = \int \rho(\mathbf{r}) \epsilon_{XC}[\rho(\mathbf{r})] F_{XC}[\rho(\mathbf{r}), \nabla\rho(\mathbf{r}), \nabla^2\rho(\mathbf{r}), \dots] d\mathbf{r}$$

The exchange energy expansion will introduce a term that proportional to the squared gradient of the density. If we considered up to fourth order, the similar term also appear proportional to the square of the density's Laplacian.

The fourth order terms in the expansion of  $F_x$  have is expressed as[30, 31]:

$$F_X(p, q) = 1 + \frac{10}{81}p + \frac{146}{2025}q^2 - \frac{73}{405}qp + Dp^2 + O(\nabla\rho^6)$$

where

$$p = \frac{|\nabla\rho|^2}{4(3\pi^2)^{2/3}\rho^{8/3}}$$

is the square of the reduced density gradient, and

$$q = \frac{\nabla^2\rho}{4(3\pi^2)^{2/3}\rho^{5/3}}$$

is the reduced Laplacian of density.

The second order gradient expansion corresponds to an expression such as:

$$E_{XC}[\rho] = \int A_{XC}[\rho]\rho(\mathbf{r})^{4/3}d\mathbf{r} + \int C_{XC}[\rho]|\nabla\rho(\mathbf{r})|^2/\rho(\mathbf{r})^{4/3}d\mathbf{r} \quad (2.4)$$

which is asymptotically valid for densities that vary slowly in space. The generalized gradient approximations (GGA) have been derived appropriate expressions by theoretical methods, and requesting that the coefficients are such that a number of formal conditions are fulfilled, and also some results in known limits are reproduced.

Another GGA approach is to fit the functional parameters in order to reproduce a number of experiment results. The results can be structural parameters, formation energies, thermochemical data, etc. This is worked well when we apply to the molecules which similar to the database. However, the transfer-ability to other systems such as solids is not guaranteed.

## 2.3 Ultrasoft Pseudo Potential

In 1990 Vanderbilt proposed smoother and highly transferable pseudopotentials called *ultrasoft* pseudopotentials [32].

The construction is started from generalized, multi-reference separable non-local pseudo potentials. Define the non-local operator such as:

$$\Delta\hat{V}_{US}^l = \sum_{i,j} D_{ij}^l \sum_{m=-l}^l |\beta_i^{lm}\rangle\langle\beta_j^{lm}|$$

where

$$D_{ij}^l = B_{ij}^l + \varepsilon_{il} Q_{ij}^l$$

then we obtain

$$\Delta \hat{V}_{US}^l = \sum_{i,j} B_{ij}^l \sum_{m=-l}^l |\beta_i^{lm}\rangle \langle \beta_j^{lm}| + \sum_{i,j} \varepsilon_{il} Q_{ij}^l \sum_{m=-l}^l |\beta_i^{lm}\rangle \langle \beta_j^{lm}|$$

The relation between all-electron and pseudo-wave function is:

$$\langle \Phi_{AE}^{ilm} | \Phi_{AE}^{ilm} \rangle_{r_c} = \langle \Phi_{PS}^{ilm} | \Phi_{PS}^{ilm} \rangle_{r_c} + Q_{ij}^l = \langle \Phi_{PS}^{ilm} | \hat{S} | \Phi_{PS}^{ilm} \rangle_{r_c}$$

where

$$\hat{S} = \hat{I} + \sum_l \sum_{i,j} Q_{ij}^l \sum_{m=-l}^l |\beta_i^{lm}\rangle \langle \beta_j^{lm}| \quad (2.5)$$

is the *non-local overlap* operator. With these definition, if the Hamiltonian is written as

$$\hat{H} = \hat{T} + \hat{V}_{PS}^{loc} + \sum_{l'} \Delta \hat{V}_{sep}^{l'} + \sum_{l'} \sum_{i,j} \varepsilon_{il'} Q_{ij}^{l'} \sigma_{m'=-l'} |\beta_i^{l'm'}\rangle \langle \beta_j^{l'm'}| \quad (2.6)$$

the pseudo-wave function  $|\Phi_{PS}^{ilm}\rangle$  are the solution of a generalized atomic eigenvalue problem

$$\hat{H} |\Phi_{PS}^{ilm}\rangle = \varepsilon_{il} |\Phi_{PS}^{ilm}\rangle + \sum_{l'} \sum_{i,j} \varepsilon_{il'} Q_{ij}^{l'} \sum_{m'=-l'}^{l'} |\beta_i^{l'm'}\rangle \langle \beta_j^{l'm'}| \Phi_{PS}^{ilm}\rangle = \varepsilon_{il} \hat{S} |\Phi_{PS}^{ilm}\rangle$$

Only the angular component  $l$  of the non-local and overlap operator produce non-zero matrix elements with well-defined state angular momentum  $l$  such as  $|\Phi_{PS}^{ilm}\rangle$ .

Then by using the Friedel sum rule we could write:

$$-\frac{1}{2} \{ [rR^l(\varepsilon, r)]^2 \frac{d}{d\varepsilon} \frac{d}{dr} \ln R^l(\varepsilon, r) \}_{r_c} = \langle \phi_{PS}^{ilm} | \phi_{PS}^{ilm} \rangle_{r_c} + Q_{ii}^l \quad (2.7)$$

which the norm of all-electron wave function should be matched with the pseudo-wave function and the diagonal element of operator  $\hat{Q}$ . By relaxing the norm-

conservation, all wave functions at different reference energies can be pseudized independently by fitting the logarithmic derivatives at the cutoff radius  $r_c$ .

## 2.4 Effective Screening Medium

ESM method describes the screening effect by introduce local relative permittivity  $\epsilon_r(r)$  and classical charge  $\rho_c(r)$  into the slab model.

The total energy expression in this model is:

$$E_{tot}[\rho_e, V] = T[\rho_e] + E_{ex}[\rho_e] - \int d\mathbf{r} \frac{\epsilon_r(\mathbf{r})}{8\pi} |\nabla V(\mathbf{r})|^2 + \int d\mathbf{r} [\rho_e(\mathbf{r}) + \rho_c(\mathbf{r})] V(\mathbf{r}) \quad (2.8)$$

Above equation express the electrostatic potential as the variational parameter.

When we introduce the Green function for the Poisson equation:

$$\nabla \cdot [\epsilon_r(\mathbf{r})] G(\mathbf{r}, \mathbf{r}') = -4\pi\delta(\mathbf{r} - \mathbf{r}')$$

Then Eq. 2.8 above, can be rewritten as

$$E_{tot}[\rho_e, V] = T[\rho_e] + E_{ex}[\rho_e] - \frac{1}{2} \int d\mathbf{r} d\mathbf{r}' [\rho_e(\mathbf{r}) + \rho_c(\mathbf{r})] G(\mathbf{r}, \mathbf{r}') [\rho_e(\mathbf{r}) + \rho_c(\mathbf{r})]$$

The Kohn-Sham equation, derived by varying the total energy with the Kohn-Sham orbital, is not affected by the ESM, but the Poisson equation, derived from electrostatic potential variation, is affected as

$$V(\mathbf{r}) = \int d\mathbf{r}' G(\mathbf{r}, \mathbf{r}') [\rho_e(\mathbf{r}') + \rho_c(\mathbf{r}')] \equiv \int d\mathbf{r}' G(\mathbf{r}, \mathbf{r}') \rho_{tot}(\mathbf{r}')$$

So the most time consuming Khon-Sham equation part is remain unchanged.

The Poisson equation in the Laue representation, is:

$$\{\partial_z [\epsilon(z) \partial_z] - \epsilon(z) g_{\parallel}^2\} G(\mathbf{g}_{\parallel}, z, z') = -4\pi\delta(z - z')$$

where  $\mathbf{g}_{\parallel}$  is a reciprocal lattice vector in the surface parallel direction and  $g_{\parallel} \equiv |\mathbf{g}_{\parallel}|$

In vacuum/slab/metal configuration which is used in this work, the boundary condition is

$$\begin{cases} V(g_{\parallel}, z)|_{z=z_1} & = 0 \\ \partial_z V(g_{\parallel}, z)|_{z=-\infty} & = 0 \end{cases}$$

$$\epsilon_r(z) = \begin{cases} 1, & \text{when } z < z_1 \\ \infty, & \text{when } z \geq z_1 \end{cases}$$

and the Green's function is

$$G^{(iii)}(\mathbf{g}_{\parallel}, z, z') = \frac{4\pi}{2g_{\parallel}} e^{-g_{\parallel}|z-z'|} - \frac{4\pi}{2g_{\parallel}} e^{-g_{\parallel}(2z_1-z-z')}$$

## 2.5 Smearing of the Fermi function

The idea of this estimation comes from the extension to LDA DFT found by Mermin. Finite temperature effects can be taken into account in the band-energy by the Mermin's approach [33]. In such kind of approaches a set of temperature-dependent electron occupations is introduced. Using an analogy of quasi-one-particles, the free energy of system at the temperature  $T$  is expressed as follows:

$$F_{\text{tot}} = \sum_i f_i(\varepsilon_i - \mu) - k_{\text{B}}TS + \Delta F + \mu N_e, \quad (2.9)$$

$$\Delta F = -k_{\text{B}}T \log \text{Tr} [\exp\{-\Delta H/k_{\text{B}}T\}], \quad (2.10)$$

where  $N_e$  and  $\mu$  are the number of electrons and chemical potential, and  $\varepsilon_i$  and  $f_i$  are the eigenvalue of band energy and its occupation number. The latter is defined as  $f_i = 1/(\exp(\varepsilon_i - \mu)/k_B T + 1)$ . Note that  $\sum_i f_i = N_e$ . The second term in Eq. (2.9) represents the entropic energy of non-interacting one-particles and  $S = \sum_i s_i = \sum_i y(f_i)$ , where  $y(x) = -x \log x + (1 - x) \log(1 - x)$ . The third term  $\Delta F$  in Eq. (2.9) represents the contributions from all the other interactions between electrons which are not included in the first (one-particle) term. Ferromagnetism is stabilized by an exchange magnetic field (molecular field) arising from the other magnetic moments. This effect is taken into account partially in  $\varepsilon_i$  and  $\Delta F$ . The magnetic dipole-dipole interaction between electrons, contributing to the SA, is included in  $\Delta F$ .

## 2.6 Magnetic Anisotropy

Magnetic anisotropy means that there is directional dependence of material magnetic properties. For example the magnetic moment direction of anisotropy material will follow its easy axis, which is have lower energy during spontaneous magnetization.

Magnetic anisotropy energy will define the strength of ferromagnet, because it related to how much energy required to rotate magnetization from the easy axis to the hard axis. In application viewpoint magnetic anisotropy play important roles, various types of magnetic anisotropy is needed in application devices whether it is weak, moderate, or strong. For example devices such as, permanent magnets, information storage media or magnetic cores in transformers and magnetic recording heads require different characteristic of magnetic anisotropy. Basically magnetic anisotropy is preferred magnetic moment orientation in materials. It's also related with internal energy that depends on spontaneous magnetization direction. It has been said that the main origin of magnetic anisotropy comes from spin-orbit coupling: In the technical

$$H_{S.O.} = \xi \mathbf{l} \cdot \mathbf{s}$$

$$\xi(r) = \frac{1}{2m^2c^2r} \frac{\partial V}{\partial r}$$

If we see in the microscopic way, there is two origin of magnetic anisotropy that is magnetostatic and electronic structure contribution. The magnetostatic contribution can be written as:

$$E_{d-d} = \frac{1}{c^2} \sum_{\mathbf{R}_i, \mathbf{R}_j}^{i \neq j} \left\{ \frac{\mathbf{m}(\mathbf{R}_i) \cdot \mathbf{m}(\mathbf{R}_j)}{R_{ij}^3} - 3 \frac{[\mathbf{m}(\mathbf{R}_i) \cdot (\mathbf{R}_i - \mathbf{R}_j)][\mathbf{m}(\mathbf{R}_j) \cdot (\mathbf{R}_i - \mathbf{R}_j)]}{R_{ij}^5} \right\}$$

This contribution was derived from dipole-dipole interaction, so the contribution depends on the arrangement of atoms, and not so depend on electric field.

As said before, the electronic structure contribution is really big to the magnetic anisotropy. This contribution due to perturbation of spin-orbit interaction, the magnetic anisotropy appears from an anisotropy of orbitals. Anisotropic occupation of the outer orbitals, for example d-orbitals will lead to magnetic anisotropy. So it is important to see the behaviour of each angular orbitals. The relation of this spin-orbit interaction is shown by:

$$H_{S.O.} = \frac{1}{2} \xi \mathbf{l} \cdot \sigma$$

## 2.7 Magnetic Anisotropy Energy

Magnetic Anisotropy energy comes from the energy difference of ferromagnet when it has different magnetic orientation, for example the energy difference between hard axis and easy axis. The anisotropy energy is come from spin-orbit coupling which break the rotational invariance with respect to the spin quantization axis [34].

Another contribution may come from magnetic dipole interaction between spins.

In practice MAE is total energy differences between in plane and out-of-plane magnetization. If the total energy differences has positive value, that means the system have perpendicular anisotropy.

The formulation of internal energy of materials is:

$$E[n_e] = K[n_e] + E_{xc}[n_e] + \int d\mathbf{r}[n_e(\mathbf{r}) + n_I(\mathbf{r})]V_H(\mathbf{r})$$

The main origin of MAE comes from the electronic structure, especially spin-orbit contribution from band electrons. The formulation is written in second order perturbation theorem:

$$MAE \propto \xi^2 \sum_k \sum_{o,u} \frac{|\langle k_o | l_z | k_u \rangle|^2 - |\langle k_o | l_x | k_u \rangle|^2}{\varepsilon_{ku} - \varepsilon_{ko}}$$

where  $ko$  is the occupied wave vector,  $ku$  is unoccupied wave vector,  $l_\alpha$  is angular momentum operator,  $\varepsilon$  is eigen value.

In order to observe EF driven magnetization reversal, we study the EF dependence of magnetic anisotropy energy (MAE). MAE is the internal characteristic of magnetic materials, which is the total energy difference between out-of-plane and in-plane magnetization. The contribution of MAE comes from dipole-dipole interaction and spin orbit interaction. In our case, the main contribution comes from spin-orbit interaction which formulated by the second order perturbation theory[35],

$$MAE \propto \xi^2 \sum_k \sum_{o,u} \frac{|\langle k_o | l_z | k_u \rangle|^2 - |\langle k_o | l_x | k_u \rangle|^2}{\varepsilon_{ku} - \varepsilon_{ko}}. \quad (2.11)$$

The coupling between the same angular orbital component in Eq. 2.11 (first summation term) will contribute to a positive MAE, while the coupling between different angular orbital component will reduce the MAE.

## 2.8 MAE from Bruno's relation

One can estimate MAEs from the orbital magnetic moments by using Bruno's formula [36]

$$\text{MAE} = \xi \frac{m_o^{[001]} - m_o^{[100]}}{4\mu_B}, \quad (2.12)$$

where  $\xi$  is the spin-orbit coupling constant (Fe: 51 meV/atom[37]) and  $m_o^{[001]}$  ( $m_o^{[100]}$ ) is the orbital magnetic moment for the [001] ([100]) magnetization direction.

### 3 Simulation Method

Density functional theory (DFT) code based on Carr-Parinello molecular dynamics has been used to perform simulation in this research. The CPVO codes [38] is built based on plane wave basis, by utilizing the ultrasoft pseudopotential and generalized gradient approximation in the exchange correlation term the many body electron problem were solved. The structural optimization is performed in scalar relativistic calculation, but finally we calculate the magnetic anisotropy energy by using full relativistic calculation, with considering spin orbit interaction.

The MAE originating from spin-orbit interaction (SOI) was estimated from the total energy difference between the different magnetization directions [100] ( $x$ -axis) and [001] ( $z$ -axis),  $\text{MAE}(\text{SOI}) = E[100] - E[001]$ , where [001] specifies the direction of film thickness. We used the  $32 \times 32 \times 1$  mesh of  $\mathbf{k}$  point sampling [39] in MAE estimation [45]. Using the scalar-relativistic level computation, in which taking a  $24 \times 24 \times 1$   $\mathbf{k}$ -mesh, we induced structural relaxation while keeping both the in-plane lattice constant and the atomic coordinates of  $O(3)$ . The MAE from the shape anisotropy,  $\text{MAE}(\text{MDI})$ , was estimated using the magnetostatic dipole interaction (MDI) and assuming the atomic magnetic moments

To understand the  $\mathbf{k}$ -space contributions to the MAE, the  $\mathbf{k}$ -resolved MAE, defined as  $\text{MAE}(\mathbf{k}) = \sum_n (f_{n\mathbf{k}}^{[100]} \varepsilon_{n\mathbf{k}}^{[100]} - f_{n\mathbf{k}}^{[001]} \varepsilon_{n\mathbf{k}}^{[001]}) + (\text{correction term})$ , was calculated, where the correction term above was assumed to be a uniform in  $\mathbf{k}$ -space and the integrated value of  $\text{MAE}(\mathbf{k})$  is equal to the  $\text{MAE}(\text{SOI})$ . After excluding the trivial contribution which is cancelled out with each other by symmetrizing  $\text{MAE}(\mathbf{k})$ . Such intrinsic  $\text{MAE}(\mathbf{k})$  is shown in Fig. 13.

### 3.1 Computational Model of Cr-buffered Fe/MgO

#### 3.1.1 Integer number of ferromagnetic layer

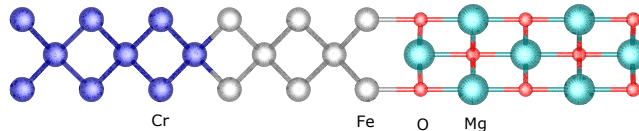


Figure 1: Schematic model of the slab systems Cr(6ML)/Fe( $x$ ML)/MgO(5ML) for  $x = 5$ .

To investigate the interface of Fe/MgO, we consider slab model consisting 0.79 nm vacuum. The construction is vacuum/Cr(6 ML)/Fe ( $x$  ML)/MgO (5 ML)/vacuum, ML means atomic monolayer. This structure are illustrated in Fig. 1. We build our computational model based on the slab model for metal. Every atom stacked in pillar-like position with two large vacuum at the both end of the model. So it has infinite 2-dimensional boundary, but with finite  $z$ -direction thickness.

In this work the thickness of Cr is already fixed to 6 ML because it has been known from previous work[41], that the thickness of buffer layer is does not effect to the estimation of MAE. 6 ML configuration assumed to be enough, also in this model we could build antiferromagnetic configuration for the Cr underlayer. Previous works show, MAE is almost independent of Cr thickness within the accuracy of  $0.1\text{mJ}/\text{m}^2$  for a given Fe thickness.

#### 3.1.2 Non-integer number of layer(Intermixing in the Fe/Cr interface)

In order to consider more detail behaviour of the magnetic anisotropy energy as a function of thickness of ferromagnet. We tried intermixing configuration or non-integer number of layer. To model this configuration, we construct  $\sqrt{2} \times \sqrt{2}$  model, also  $2 \times 2$  in-plane lattice constant model. Therefore we can reproduce such 25%, 50%, or 75% intermixing at the Fe/Cr interface model, just like described in Fig. 2

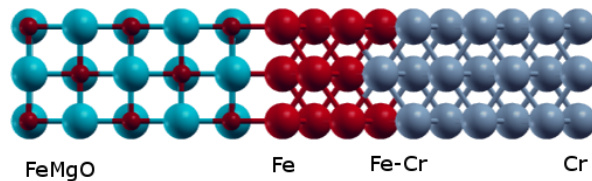


Figure 2: Schematic model of the slab systems Cr(6ML)/Fe( $x$ ML)/MgO(5ML) for  $x = 3.5$ .

### 3.1.3 Smearing effect of the temperature dependence

The magnetic anisotropy also depends on the magnetic moment. As temperature of the magnetic moment decreases, the anisotropy energy often becomes decreased. The main part of such reduction may be realized by the contribution of SA. The temperature dependence of the magnetic moment originates from the spin fluctuations. In order to evaluate it, one can take a method based on the microscopic electronic structure [23, 24]. However, for focusing the smearing effect at the Fermi level and for simplicity, this work employs a well-known sophisticated model as the temperature-dependent magnetization  $M(T)$ , as follows:  $M(T) = M_0 y(T/T^*)$ , where  $y$  is a given function,  $M_0 = M(0)$ , and  $T^*$  is a sophisticated parameter, such as Curie temperature ( $T_c$ ).  $T^*$  is used as a sort of fitting parameters. In this work, due to the thinner magnetic slab, we employed  $y(T/T^*) = 1 - (T/T^*)^2$  [29].

The magnetic anisotropy energy is presented as  $K = K_b + K_{sa}$ , where  $K_b$  is from the band energy and  $K_{sa}$  from the SA.  $K_b$  is expressed as the energy difference of free energy  $F_b$  between the different magnetization directions, such as [100]( $x$ -direction) and [001]( $z$ -direction). The  $F_b$  is given as follows [42, 43] :

$$F_b = \sum_{n\mathbf{k}} f_{n\mathbf{k}} (\varepsilon_{n\mathbf{k}} - \mu) - k_B T S + E_d + \mu N_e, \quad (3.1)$$

where  $E_d$  is the double counting term in the total energy.[44] Using Eq. (3.1),  $K_b = F_b^{[100]} - F_b^{[001]}$  [45]. The  $K_{sa}$  is expressed as  $K_{sa} = -\mu_0 M^2 / 2\Omega + \Delta K_{sa}^{\text{int}}$ , where

$\Omega$  and  $\mu_0$  are the volume of magnetic slab and permeability of vacuum, respectively, and  $\Delta K_{\text{sa}}^{\text{int}}$  is the interface contribution which does not include in the 1st term.  $\Delta K_{\text{sa}}^{\text{int}}$  originates from both the discreteness of stacking atomic layers [46] and the deviation from spherical atomic spin moment density at the interface magnetic atoms [47]. These are due to the shape of magnetization distribution, reducing the in-plane SA in ferromagnetic Fe layers.

In the demonstration, we used the slab system, vacuum(0.79nm)/Cr(6ML)/Fe(5ML)/MgO(5ML)/vacuum(0.79nm) (ML=atomic monolayer). At the Fe/MgO interface the Fe atom was placed just next to the O atom due to its stability, and in the Cr and Fe layers the body-centered layer-stacking sequence was used. The in-plane lattice constant extracted from bulk Cr was employed.

## 3.2 Computational Parameter

The calculation perform in custom built DFT Code named CPVO. In this program we use below parameter:

- 30 Ryd cutoff wave function.
- 300 Ryd cutoff charge density.
- GGA exchange correlation
- Ultrasoft pseudo-potential
- 32x32x32 dense k-points, and 24x24x1 sparse k-points
- Spin orbit interaction when calculating MAE

The density functional calculation employs a fully relativistic (with spin-orbit interaction) ultrasoft pseudopotentials and planewave basis [48], by using the generalized gradient approximation [49]. We used a  $32 \times 32 \times 1$  (sparse) mesh for the  $\mathbf{k}$  point sampling in the estimations of  $K_{\text{b}}$ . At the low temperatures, unfortunately,

the sparse mesh mentioned above cannot give any convergence in the self-consistent calculation, and a  $64 \times 64 \times 1$  (dense) mesh was also introduced. The difference from the sparse mesh appeared at the low temperatures, such as less than or equal to 100-200 K, and becomes small at 300 K. The dense mesh requires a large amount of computational source so that the number of calculated temperature points were limited to a few.

### 3.3 Workflow

Here we briefly describe the work flow of the experiment which conducted to write this dissertation report. The experiment basically performed in two stage in order to finally get the MAE and electronic structure. The first stage we call it the collinear stage, and non-collinear for the second stage.

Fig. 3 describe how the experiment in density functional simulation is performed in this work. First we treat the electron optimization (OPTE1) under small amount of magnetic field bias to set the magnetic orientation under the scalar-relativistic calculation, then the bias canceled after several iteration. Calculation continue with next electronic structure convergence (OPTE2) after canceling the presence of magnetic field, then then the atomic structure is optimized (OPTS). We call this step is the optimization in collinear condition as described in Fig. 3. The electron convergence are performed in the first stage is to get the optimized electronic structure at initial atomic configuration. After that we perform structural relaxation in non-relativistic condition (OPTS), the optimization is performed until the atomic force low enough. When the optimized atomic structure achieved, we optimize the electronic structure one more time (OPTE3). After the final optimized electronic structure is achieved, it used to draw the density of states and band dispersion of interested atom.

After the optimization of atomic and electronic structure in collinear condition, we continue the calculation in the non-collinear magnetic structure. The atomic

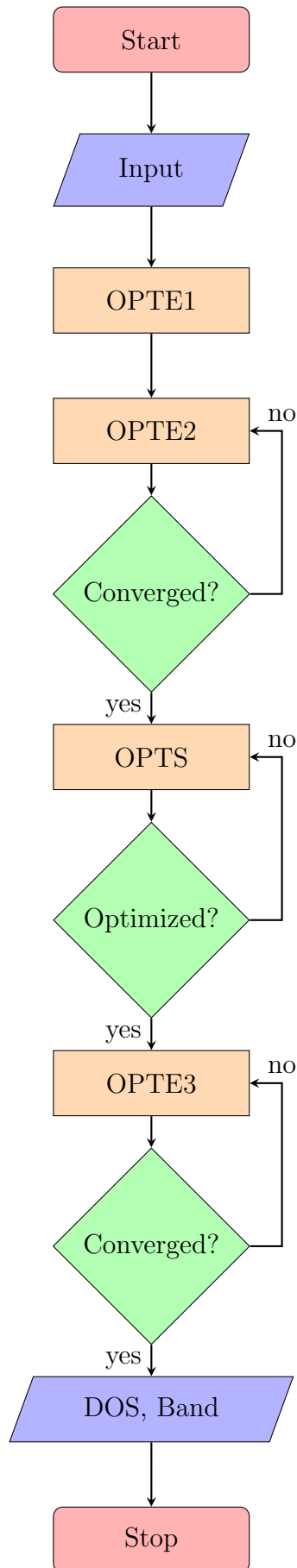


Figure 3: Research workflow in generating electronic structure of the target material in Collinear Calculation

---

structure received from previous optimized structure are being used and first stage of OPTE1 performed by using relativistic effect. In this OPTE1 we put small bias on magnetic field to set the spin structure on the thin film. The small imposed bias are given to make the [001] orientation of the ferromagnet, and also make the Cr in antiferromagnet configuration. After we take off the bias, convergence of electronic structure are continued (OPTE2). When we reach the lowest level of convergence in this electronic structure, we take this configuration as the out of plane magnetization. Therefore we need to rotate the spin orientation, especially the ferromagnet to be in-plane orientation. We call the procedure as the SPINSET. Finally we measure the difference of the energy between in-plane and out-of-plane orientation. All of this process are summarized in Fig. 4.

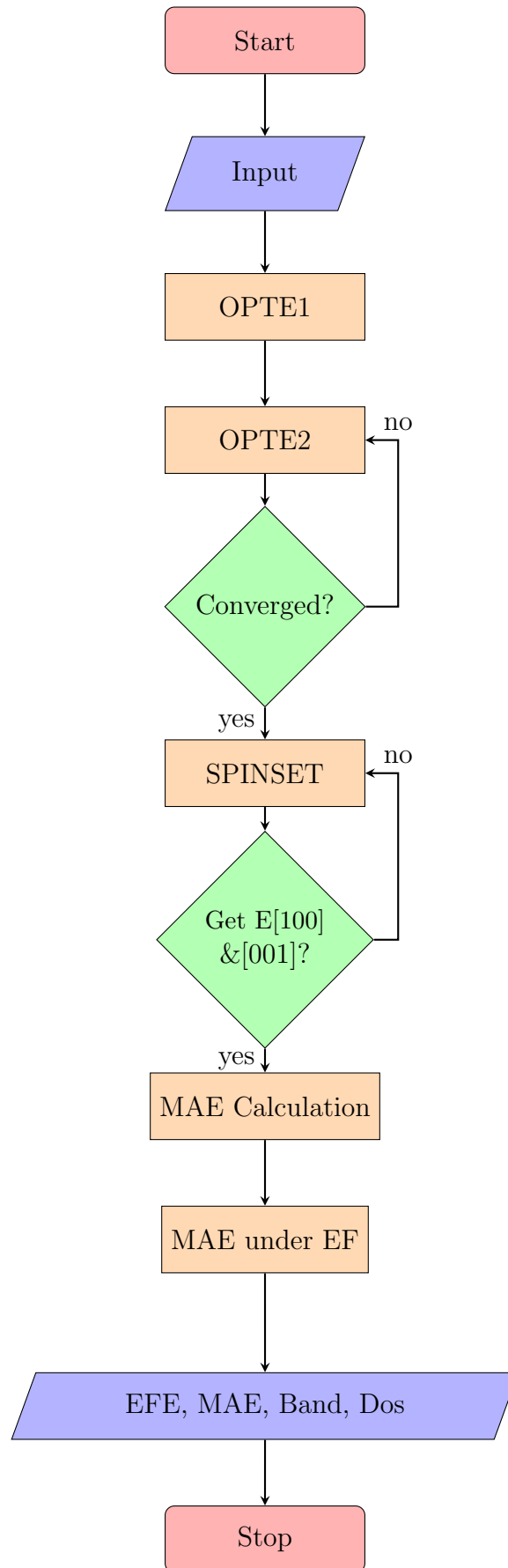


Figure 4: Research workflow in generating electronic structure of the target material in Non-collinear Calculation

## 4 Result and Discussion

### 4.1 Investigation on large perpendicular magnetic anisotropy energy

Within this chapter we will explore the result when we change the thickness of ferromagnet materials. The Cr-buffer effect to the electronic structure of the interface states will be explained.

#### 4.1.1 MAE(SOI)

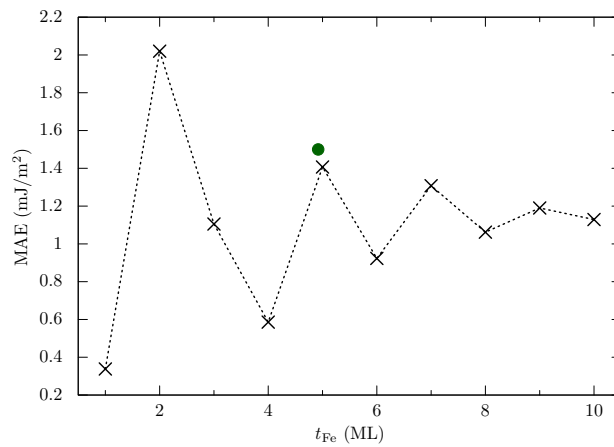


Figure 5: Thickness dependence of the magnetic anisotropy energy (MAE) from spin-orbit interaction in Cr/Fe( $x$ ML)/MgO. The bullet indicates the experimental value (ref. [50]), where 1ML thickness is assumed to be 0.142 nm.

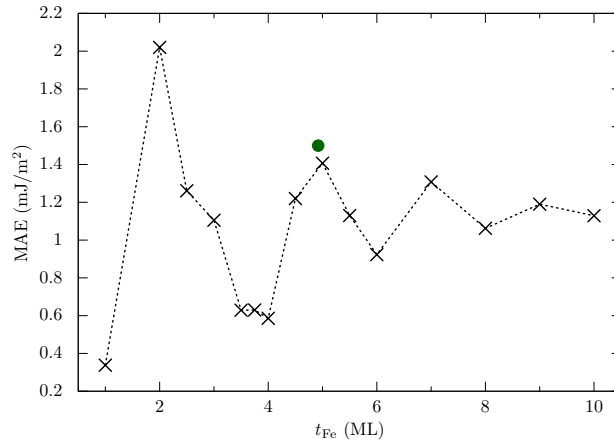


Figure 6: Thickness dependence of the magnetic anisotropy energy (MAE) from spin-orbit interaction in Cr/Fe( $x$ ML)/MgO. In this model we also consider the non-integer layer, where intermixing is possible. The bullet indicates the experimental value (ref. [50]), where 1ML thickness is assumed to be 0.142 nm.

We report the thickness dependence of MAE(SOI) in Fig. 5. It indicates an oscillating perpendicular anisotropy with respect to Fe thickness ( $x$ ), and the maximum of 2.0 mJ/m<sup>2</sup> at Fe 2ML( $x = 2$ ) and other maximal values at 5ML( $x = 5$ ) and 7ML( $x = 7$ ). The behavior shows that an odd-even alternating oscillation at the thicker systems (4ML-10ML). For the thinner systems, the amplitude of oscillation is largely enhanced since large changes are expected in the electronic structure around the Fe/MgO interface.

The estimation to the MAE of non-integer layer also performed in order to see the behaviour. Fig. 6 showed that the oscillation tendency as the thickness increase is not changed, all the non-integer estimation is located at the intermediate value of MAE from integer layer thickness.

#### 4.1.2 Fe 2ML case

The maximum MAE at Fe 2ML is much larger than the previous theoretical and experimental values in the Fe/MgO interface family, comparable to the interface contribution extracted from the extrapolation fitting in the experiment [16]. At Fe 5ML our value agrees well with the experimental value [50].

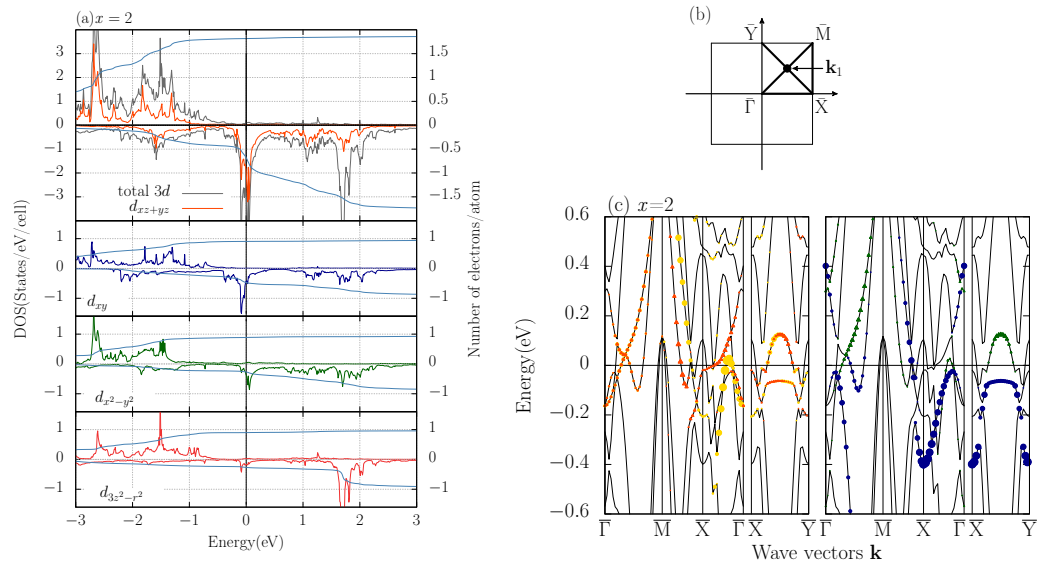


Figure 7: Electronic structures at the Fermi level in Cr/Fe(2ML)/MgO without including spin-orbit interaction, (a) projected densities of states (PDOS) (from the top) 3d total  $d_{xz+yz}$ ,  $d_{xy}$ ,  $d_{x^2-y^2}$ ,  $d_{3z^2-r^2}$  components, (b) selected  $\mathbf{k}$ -point path, and (c) band dispersion for the Fe 3d orbitals at the interface Fe(1)

Fig. 7 shows the projected density of states (PDOS) at the interface in  $x = 2$  and band dispersions with  $3d$  orbital components in the vicinity of the Fermi level ( $E_F$ ). As shown, the  $E_F$  is located between the two peaks of PDOS consisting of  $3d$  orbitals. These electronic states are relatively localized since the main orbital components are made of the non-bonding  $3d$ -orbitals. Indeed, the states form a flat band around the  $\mathbf{k}_1 = \pi/a(1/2, 1/2)$  (see Fig. 7) and a saddle point near  $\mathbf{k}_1$  in two-dimensional Brillouin zone (2DBZ). The band flatness appears along  $\bar{X}-\bar{Y}$  line in 2DBZ. These features are remarkably observed for both the occupied and unoccupied bands in Fig. 7(c). There is a saddle point nature around  $\mathbf{k}_1$  in 2DBZ (not exact of saddle point). Along  $\bar{X}-\bar{Y}$ , there is a maximum at  $\mathbf{k}_1$  in the  $3d$ -orbital band just above  $E_F$ , and simultaneously along  $\bar{\Gamma}-\bar{M}$  a minimum near  $\mathbf{k}_1$ .

This feature is the origins of sharp PDOS peaks in the interface states, appearing more or less in the Fe/MgO and its family systems. However, for realizing such features, there may be a combination of two conditions. The one is an appropriate orbital hybridization between 1st Fe and 2nd Fe layers. This keeps splitting the mixed eigenstates of  $d_{xz}$  and  $d_{yz}$  components at  $\bar{M}$  point to the lower and higher eigen energies, while in the Fe 1ML system, those stays remain on or around  $E_F$  [35]. The 2nd condition is also an orbital hybridization between Fe  $d_{3z^2-r^2}$  and O  $p_z$ . This keeps the  $d_{3z^2-r^2}$  away from  $E_F$ , not disturbing the localized states of non-bonding  $d_{xy}$ ,  $d_{x^2-y^2}$ ,  $d_{xz}$ , and  $d_{yz}$  at  $E_F$ . The latter has been well known as one of important origins for realizing perpendicular anisotropy [2]. This is because the orbital  $d_{3z^2-r^2}$  always contributes only to in-plane magnetic anisotropy, assuming that the contribution from the majority spin state can be neglected due to a large exchange splitting [35]. The MAE maximum in Fe 2ML is obtained as the consequences of the origins discussed above. Note that there are vertical couplings of SOI around  $\mathbf{k}_1$  area in 2DBZ, which contribute to perpendicular anisotropy; couplings of  $d_{xy}-d_{x^2-y^2}$  and  $d_{xz}-d_{yz}$ .

### 4.1.3 Fe 5ML case

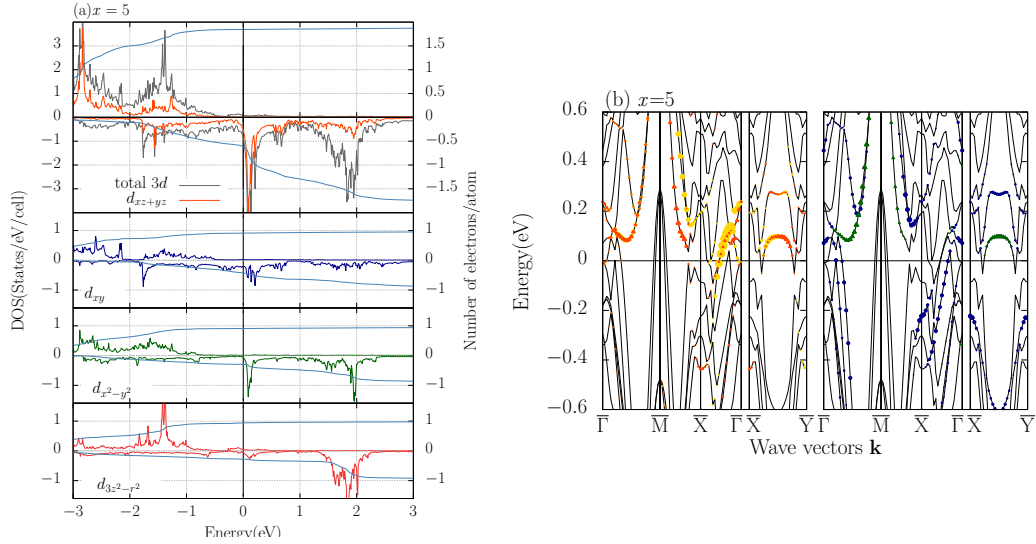


Figure 8: Electronic structures at the Fermi level in Cr/Fe(5ML)/MgO without including spin-orbit interaction, (a) partial density of states (PDOS), (b) band dispersion for the Fe 3d orbitals at the interface Fe(1)

In  $x = 5$ , such dispersionless states is more clearly observed just above  $E_F$  (0.1 eV in Fig. 8(c)), the band changes upward along  $\bar{\Gamma}-\bar{M}$  and slightly downward along  $\bar{X}-\bar{Y}$ . In the more real-life scenario of  $x = 5$  configuration in Fig. 8, the formation of interface state is also observed, but unfortunately the vertical coupling of  $d_{xy}-d_{x^2-y^2}$  and  $d_{xz}-d_{yz}$  at  $\mathbf{k}_1$  is already shifted away from the Fermi level to higher energy. Therefore we have lower value in the magnetic anisotropy energy, but we still have the coupling of  $d_{xz}-d_{yz}$  orbital at middle point of  $\bar{X}-\bar{\Gamma}$  and  $\bar{\Gamma}-\bar{M}$  which is contribute significantly to the perpendicular magnetic anisotropy.

### 4.1.4 Thickness dependences of interface electronic structure and number of electrons

The thickness dependence in MAE has a relationship with the number of electrons (NOE) in the 3d orbital of minority spin state on the interface Fe. In the large

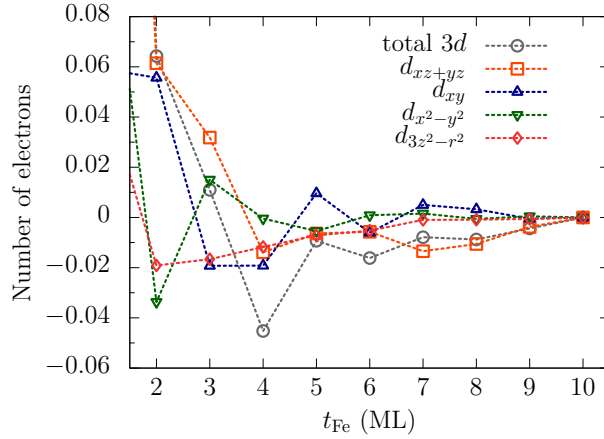


Figure 9: Thickness dependence of the number of 3d electron on the interface Fe. The relative values with respect to those of Fe 10ML are shown. The colors of grey, orange (yellow), blue, green, and red are used for total 3d orbital,  $d_{xz+yz}$ ,  $d_{xy}$ ,  $d_{x^2-y^2}$ , and  $d_{3z^2-r^2}$ , respectively.

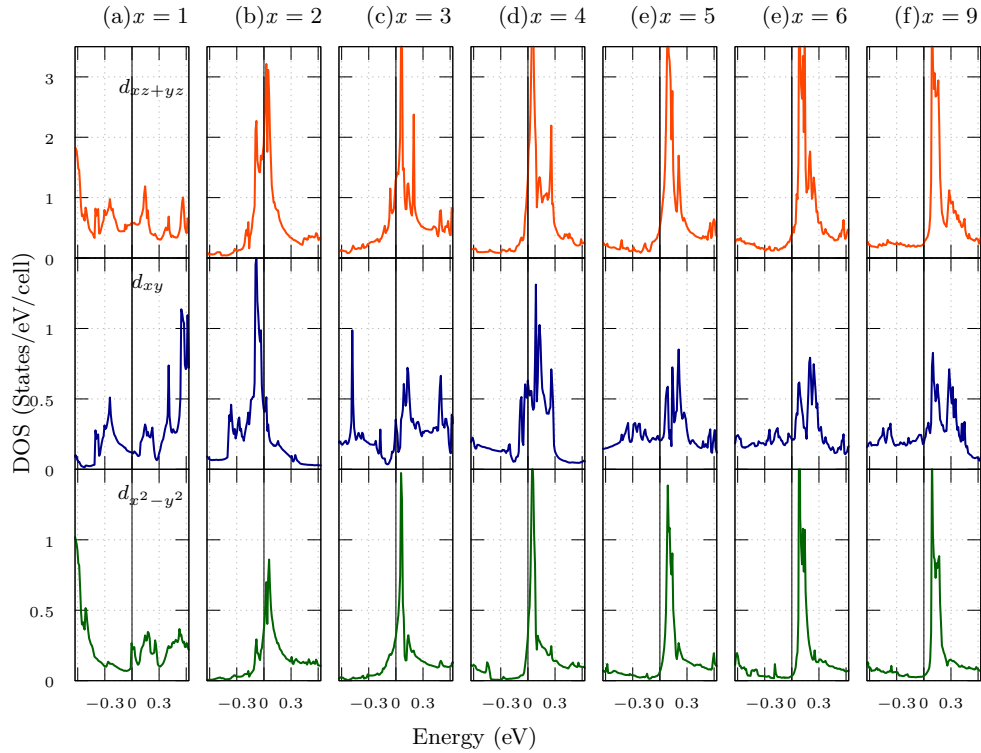


Figure 10: Projected density of states (PDOS) for the interface state in Cr/Fe( $x$ ML)/MgO; (a)–(g) for  $x = 1 - 6$  and 9, respectively. The top, middle, bottom lows in the panels show the components of  $d_{xz+yz}$ ,  $d_{xy}$ , and  $d_{x^2-y^2}$ .

variation range of MAE ( $< \text{Fe 4ML}$ ), the NOE decreases as thickness, and in the odd-even alternating range ( $\geq \text{Fe 4ML}$ ) its NOE does not synchronize so much with the MAE, as shown in Fig. 9. For the former, the number of Fe works as hole doping, while in the latter the MAE may be influenced by the details of electronic structures at the interface. Interestingly, note that the NOEs of  $d_{xy}$  and  $d_{x^2-y^2}$  show an alternating behavior in their relative values (See Fig. 9). Indeed, the alternating nature appears at the  $d_{xy}$  component in the band dispersions (not shown) and PDOS (see Fig. 10).

The number of  $3d$  electrons at the interface Fe is summarized in Fig. 9. The total number of  $3d$  electron decreases as the thickness increases until Fe 4ML. This decrease is in accordance with the relationship of electronegativity between Fe and Cr. The electrons on Fe of larger electronegativity gradually increases as the thickness of Fe increases from Fe 4ML.

Fig. 10 shows the series of PDOS for interface states. Except for  $x = 1$ , the sharp peaks appear, implying the localized nature of wave functions. It is worthy to notice that the series of  $x = 2 - 5$  do not show a simple rigid band filling. The shape of  $d_{xy}$  component changes while that of  $d_{x^2-y^2}$  is kept without any large change. In details, the peaks of  $d_{xy}$  and  $d_{x^2-y^2}$  are located just below and above the  $E_F$  level, respectively, in Fe 2ML, and as the thickness the peaks of  $d_{xz+yz}$  moves to higher energies with that of  $d_{x^2-y^2}$ . Additionally, it is interesting to see the PDOS peak sharpen in the thicker systems (see the case of  $x = 9$ ). The origin of interface states energy shift is speculated as an orbital hybridization with the Cr underlayer. At the Cr/Fe interface, the  $3d$  orbital components at  $E_F$  was shifted due to the hybridization to a higher energy for Cr and to a lower energy for Fe. This realizes the electron transfer from Cr to Fe atoms, showing a property of smaller electronegativity for Cr. Consequently, the  $3d$  orbital on the Fe of Fe/MgO interface can get electrons as the thickness of Fe layer decreases. Indeed, it was observed clearly in the Fe layer with small  $x$ 's as a vicinity effect of Cr. Interestingly, the similar energy lowering of

IS occurs as the decrease of in-plane lattice constant [51], inducing the modulations in MAE.

#### 4.1.5 Variation of the atomic magnetic moment

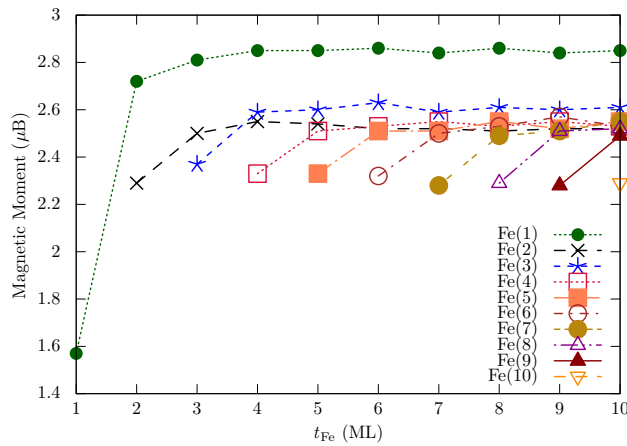


Figure 11: Atomic magnetic moment of Fe in the ferromagnet layer, Fe(1) are located at the interface of MgO.

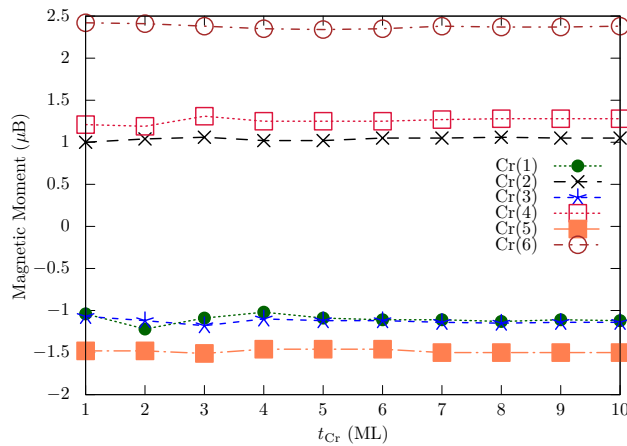


Figure 12: Atomic magnetic moment of Fe in the ferromagnet layer, Cr(1) are located at the interface with Fe.

We report the results of atomic magnetic moments obtained by integrating the spin density in the atomic sphere with the radius (Cr: 0.90 Å, Fe: 0.90 Å), as shown in Fig. 11 and Fig. 12. As general trends the Fe magnetic moment is enhanced ( $2.8 \mu_B$ ) and reduced ( $2.3 \mu_B$ ) at the Fe/MgO and Cr/Fe interfaces, respectively, compared with those of the inside layers ( $2.5 \mu_B$ ). In the Cr layer, the magnetic moments

couples also antiferromagnetically between the neighboring layers. These configurations are similar to the previous theoretical work on the Fe(001)/MgO/Cr/Fe magnetic tunnel junctions [52]. Note that the magnetic alignment related with the Cr atoms has not been known in the thin film materials (devices). To bulk Cr, an incommensurate antiferromagnetic spin-density wave has been known for a long time [53] and the interface with Fe may possibly show a noncollinear magnetic configuration [54].

As shown in Fig. 12, the magnetic moment on Cr(6) is larger than those of the other Cr MLs, because this atom faces to vacuum and the electron wave function is more localized near the vacuum. This feature contributes to larger magnetic moment.

#### 4.1.6 The $\mathbf{k}$ -resolved anisotropy

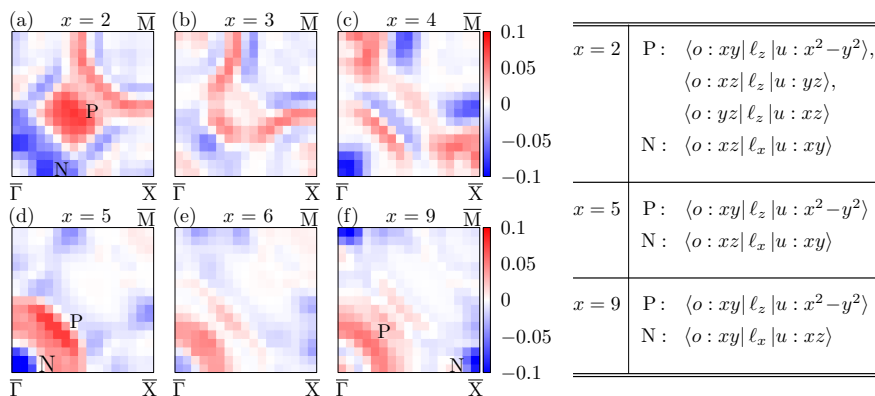


Figure 13: The  $\mathbf{k}$ -resolved contribution of MAE:  $\text{MAE}(\mathbf{k})$  for  $x = 2, 3, 4, 5, 6, 9$ , which corresponds from (a) to (f), respectively. The red (blue) color indicates positive (negative) contribution to the MAE from electronic band structure. The non-vanishing typical couplings are described in the right hand side for the positive (negative) area indexed by P (N) in (a)( $x = 2$ ), (d)( $x = 5$ ), and (f)( $x = 9$ ), where the symbol  $o$  (symbol  $u$ ) specifies the states below (above) the Fermi level, and the  $\ell_z$  ( $\ell_x$ ) is the operator of  $z$ -component ( $x$ -component) orbital angular momentum.

In order to understand the contribution to perpendicular magnetic anisotropy from the second order perturbation clearly. We develop tools to analyze the dis-

tribution of magnetic anisotropy energy in the  $k$ -space. As observed in Fig. 13 we can see in the thicker Fe layer ( $x = 9$ , see Fig. 13(f)), there is some positive contribution (red area) along the line  $k_x + k_y \sim \frac{2\pi}{a} \times q$  ( $q = 0.22$ ). This contribution survives overcoming the negative contributions (blue area) in the other area. Such positive contribution commonly appears, enhanced in  $x = 5$  (Fig. 13(d)) and  $x = 2$  (Fig. 13(a)). For  $x = 2$ , in addition, the positive area is much extended to the area of larger  $q$ -values. These characters may cause the large MAEs in the systems of  $x = 2, 5$ . Along the line mentioned above ( $q = 0.34$ ), in contrast, some cancellation appears in  $x = 4$  (Fig. 13(c)). In the case of  $x = 2$  the large MAE may be attributed to the area near  $\mathbf{k}_1$  where the flat band and singularity appear, through the consideration of second-order perturbation theory,[35] as discussed in the previous paragraph. In Fig. 13, the coupling which may contribute to the enhanced MAE is presented for the positive area (indexed by the symbol P). Even in  $x = 5, 7, 9$ , those vicinities of flat band and singularity can enhance the positive contribution in MAE (see Fig. 5) and are consistently explained with MAE( $\mathbf{k}$ ) (not shown here for  $x = 7$ ).

#### 4.1.7 Total magnetizations

In the theoretical approach we obtained the magnetic dead layer (MDL) with 0.053 nm thick at most, while the experiment clearly showed the MDL with 0.1 nm thick [16]. The theoretical magnetization is larger than the experimental one by about 24 % at the Fe 5 ML, as shown in Fig. 14. These differences could be ascribed to an alloying effect at the Cr/Fe interface in the experiment. This allows to draw a suppression of the in-plane anisotropy from MDI contribution, or alternatively an enhancement in the strength of interface perpendicular anisotropy. The nearest neighbor pairs of Cr–Cr and Fe–Cr tends to enhances antiferromagnetic coupling between the magnetic moments, and possibly inducing a noncollinear magnetic structures due to a competition in magnetic couplings [54]. Associated with such

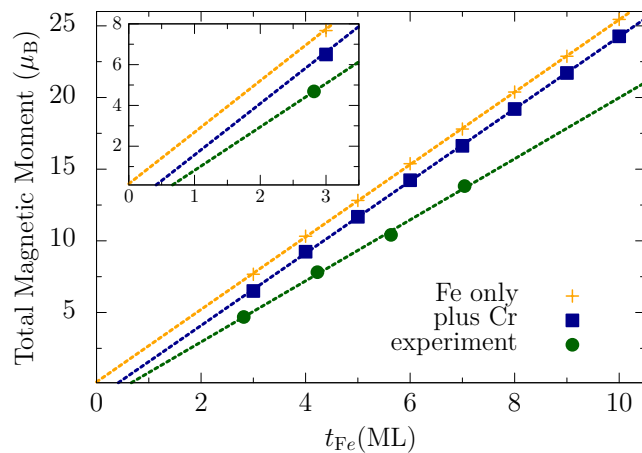


Figure 14: Thickness dependence of magnetizations, compared with the available experimental data(ref. [16]). Plus symbol indicates total magnetizations contributed from Fe atom only, solid box includes the contribution of Cr, bullet indicates experimental data.

complexity in magnetic configuration, the MAE(SA) modulates due to the change in MDI.

#### 4.1.8 Shape anisotropy

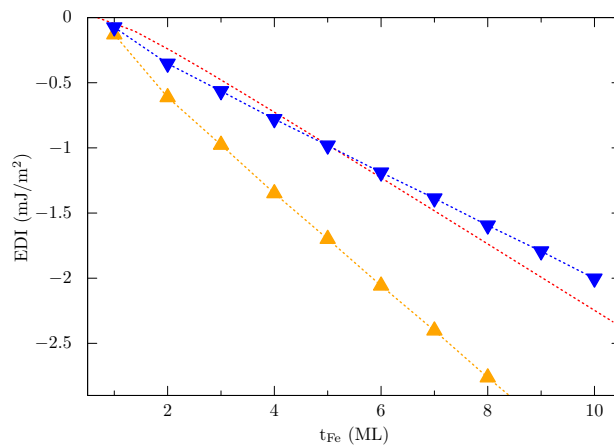


Figure 15: Theoretical MAE(MDI) (yellow triangles), normalized MAE(MDI) (blue reverse triangles), and experimental MAE(SA) (red dots), the dashed lines are only guide.

The shape anisotropy is realistically important for determining the whole magnetic anisotropy. When we compare our MAE(SOI) with those from measurements, the

shape anisotropy needs to be estimated precisely. Here, we estimated the shape anisotropy energy, MAE(SA), in two ways; from the MDI [55] using the theoretical atomic magnetic moments and the estimation  $(-\mu_0 M_s^2/2)$  using the experimental saturation magnetization ( $M_s$ ) [16]. In the former, all the Cr layer were also taken into account. This shape anisotropy contribute to the in-plane component, large negative value means more reduction to the MAE(SOI). So we could observe that the calculation from pure dipole-dipole interaction [55] provide much reduction compared to the one extracted from experimental ones [16]. Just as described in Fig. 14, the estimation of total magnetization are overestimate experimental value, therefore we consider the case of normalized ones. Later we can use this value as the corrected factor of the MAE(MDI).

#### 4.1.9 Total MAE

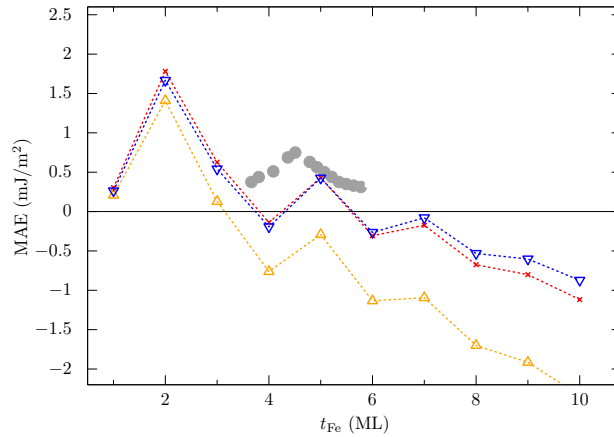


Figure 16: Total magnetic anisotropy energy (MAE), compared with the experimental data (bullets)(ref. [16]). The open yellow triangle symbol specifies the data estimated theoretically; MAE(SOI)+MAE(MDI), the reverse blue triangle symbol represent the MAE(SOI+MDI) after the 26% reduction of theoretical atomic moment, and the cross data the sum of the theoretical MAE(SOI) and the shape anisotropy MAE(SA) estimated using the experimental magnetization.

Fig. 16 reports the total MAE, namely summation of MAE(SOI) and MAE(SA), in comparison with the available experimental data. This figure shows that our estimation is much reduced due to large in-plane contribution from the MDI. As

shown in Fig. 15, the experimental MAE(SA) is much reduced in absolute, compared with the theoretical one. This is an origin why we have so much reduced value. By considering the reduced MDI (rMDI), we could obtain that the MAE (SOI+rMDI) describe in the blue reverse triangle. In this result we could observe an agreement with the experimental data [16].

#### 4.1.10 Thickness dependence of electric field effect

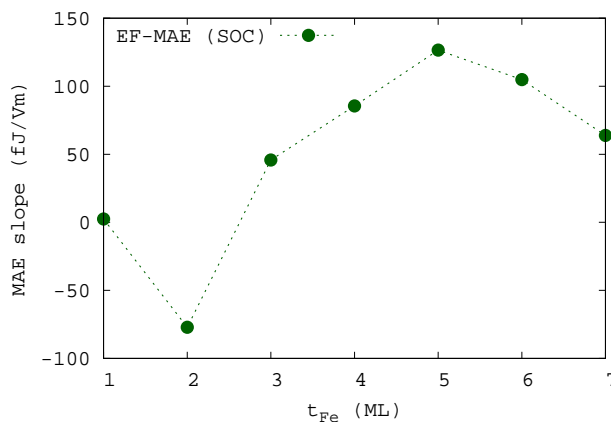


Figure 17: The electric field effect change as the thickness of the ferromagnet increase

In Fig. 17 we observe the change of EFE constant as the thickness of ferromagnet increase. The modulation of thickness change the EFE significantly especially for the case of thinner than 5ML of ferromagnet. EFE constant for each layers are become saturated in positive value above 50 fJ/m<sup>2</sup> for thicker layer case. But for 2ML case, the value of this EFE become negative, in the opposite sign compared to the other systems investigated in our calculation.

#### 4.1.11 Bruno's relation to the MAE

The obtained MAE(SOI) result can be compared to Bruno relation [56] in order to confirm the validness of our calculation results. In Fig. 18 we can observed that in even number of ferromagnet layers MAE(SOI) can be fairly close estimated by assuming 62 meV to the spin-orbit coupling constant. But the Bruno's model

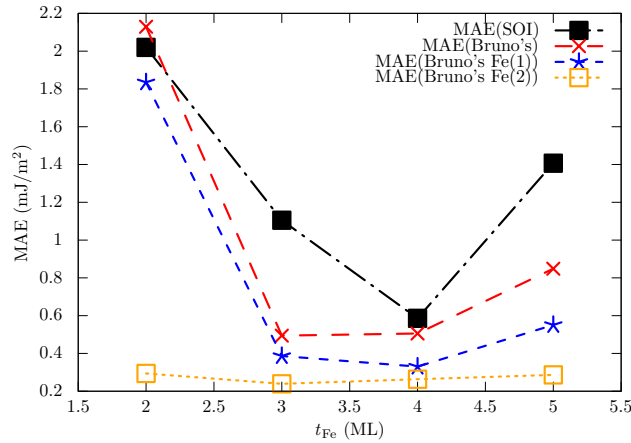


Figure 18: The estimation from Bruno's relation compared to the calculation of MAE from SOI. Black solid square represent MAE from SOI, red cross symbol are MAE calculated from Bruno relation, blue star symbol are the contribution from Fe(1) at the interface, and orange empty square symbol are contribution from Fe(2).

is much underestimated the MAE for odd number of Fe cases. This features can be tolerated, because its already known even this relation are applied to most of the ferromagnet transition metals like Ni, Fe, Co, sometimes due to complexity of the system or the large value of spin-orbit coupling constant this relation can't be filled. In another way, it might be this model is too simple for even number of Fe layers cases. Still we could expect the same out-of-plane tendency for the number of MLs in Fig. 18. We could consider the main contribution of magnetic anisotropy energy come from the first layer of interface iron with the MgO. The contribution of nearest neighbor is constant around  $0.2 \text{ mJ/m}^2$ , and the contribution from next nearest neighbor is almost zero, therefore not included in the Fig. 18.

#### 4.1.12 The thermal stability of thin layers of ferromagnet

In the case of consideration when we decrease the thickness of Fe layer, for example become 2ML, the ferromagnetic state may become unstable against thermal disturbance. This could be denied in a discussion of Cr-Fe magnetic interaction. The Fe at the Cr/Fe interface has a strong antiferromagnetic interaction of Heisenberg type. This stabilizes the ferromagnetic state of Fe thin layer. The previous works reported

large exchange interactions of  $J = 69$  meV and  $|J|=59, 20$  meV for Fe-Fe and Cr-Fe nearest neighbors, [54, 57, 58] respectively. They could be enough to maintain the ferromagnetic states at room temperatures. However, practically, associated with the existence of magnetic dead layer in such system, [16] Fe atom may diffuse into the Cr layer during the fabricating process at high temperatures. Indeed, when exchanging the Fe and Cr atoms at the Cr/Fe interface in Fe 4ML, the total energy does not become so higher (50 meV/in-plane Fe).

#### 4.1.13 The origin of oscillating behaviour: Interface states and Quantum well

As shown in Figs. 7 and 10 the interface state discussed here is presented just as some sharp peaks in this work. The main body of states is on  $E_F$  or just above  $E_F$  by less than 0.2 eV. These energy levels are located at the same energy range in which the enhanced magnetic tunneling spectra appears [50]. The interface states in the present work may have the potential to make a state resonating with the conduction electron through the  $s-d$  interaction at the interface [59]. Indeed, the enhanced spectra in the spin-dependent tunnel conductance has been observed, implying some unknown/non-resolved mechanism behind [60, 3].

The Fe layer, forming a quantum well structure, is terminated at the Fe/MgO and Cr/Fe interfaces, calling the amplitudes of wave function at the edges have a feature of odd-even alternating behavior in the one dimensional model chain of which the atomic site is connected with electron transfer integral. The  $d_{xy}$  component at the Fe/MgO interface is largely affected due to its non-bonding nature, and can be sensitive to external perturbation from the other edge of Cr/Fe interface. The electron transfer between the  $d_{xy}$  orbitals of neighboring Fe MLs is proportional to  $T_{xy,xy}(\mathbf{k}) \sim e^{i\mathbf{k}\cdot\mathbf{R}}\{3t(dd\sigma) + 2t(dd\pi) + 4t(dd\delta)\}/9$ , and is not negligible because the absolute of transfer integral can reach to about 0.1 eV [35]. Consequently, as an edge effect of the model chain, some non-negligible changes of  $d_{xy}$  are supposed to

appear at the interface states.

## 4.2 Fermi level smearing effect to the MAE

### 4.2.1 Magnetic anisotropy from spin-orbit interaction

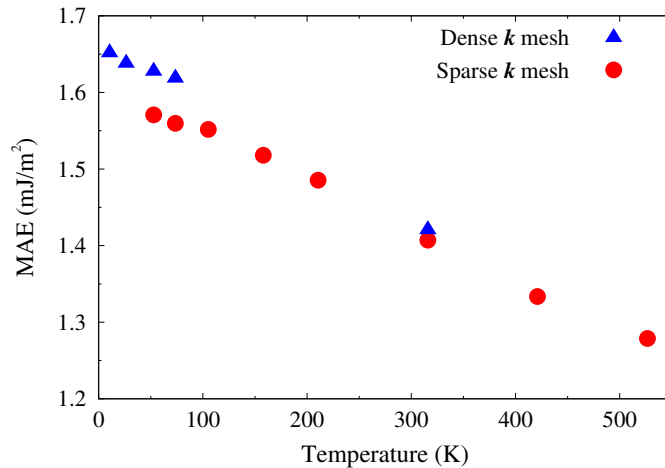


Figure 19: Fermi level smearing effect in magnetic anisotropy energy (MAE) with respect to temperature. The symbols of triangle and circle specify the data by dense and sparse meshes, respectively.

Fig. 19(b) shows  $K_b$  per unit area as a function of  $T$ . These values are positive, contributing to a perpendicular magnetic anisotropy as expected in a family of Fe/MgO interfaces [1, 7, 2], and similar to the data ( $1.5 \text{ mJ/m}^2$ ) from the experimental measurement at the room temperature for the Fe thickness ( $t_{\text{Fe}}$ ) of  $0.7 \text{ nm}$  [50]. Such positive contribution may be attributed to the SOCs between the orbital components of  $d_{xy}$  and  $d_{x^2-y^2}$ , or  $d_{xz}$  and  $d_{yz}$  in the respective occupied and unoccupied states [61]. The smearing effect decreases  $K_b$  monotonically by  $0.38 \text{ mJ/m}^2$  from  $10.5 \text{ K}$  to  $527 \text{ K}$ . This decreasing quantity is not negligible, implying one of important ingredients for the temperature dependence of magnetic anisotropy.

### 4.2.2 Electronic structure

$K_b$  decreasing with temperature is a consequence of electronic structure. To confirm the variation property, in Fig. 20 we show the band dispersion curves and the partial

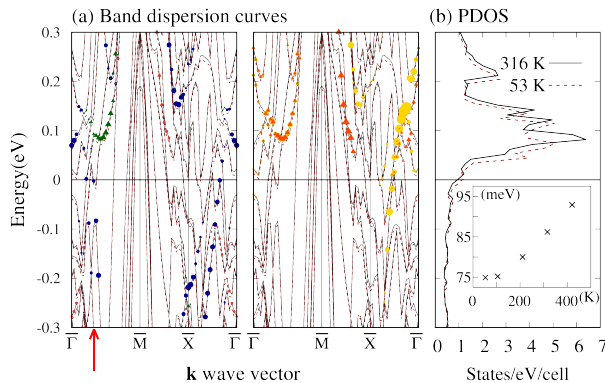


Figure 20: (a) Band dispersion curves (left and center) and (b) partial density of states (PDOS) for the minority-spin-state 3d orbital on the interface Fe in the [001] magnetization system determined with the temperature-dependent Fermi level smearings of 316 K (full curves and symbols) and 53 K (broken curves). The symbols specify the angular orbital components projected on the interface Fe atoms;  $d_{xy}$ ,  $d_{x^2-y^2}$ ,  $d_{3z^2-r^2}$  (left) in blue, green, and red bullets, respectively, and  $d_{xz}$ ,  $d_{yz}$  (center) in orange and yellow. The Fermi levels are adjusted to zero in the vertical axis with the horizontal full line, and the Fermi energy (chemical potential  $\mu$ ) decreases by 0.11 eV as temperature. The inset figure in (b) shows the typical data of  $\varepsilon_{n\mathbf{k}} - \mu$  with respect to the temperature at  $\mathbf{k} = 0.33 \times \Gamma\bar{M}$  (vertical red arrow).

density of states (PDOS) for two different temperatures (53 K and 316 K). The eigenvalue with respect to the chemical potential ( $\varepsilon_{n\mathbf{k}} - \mu$ ) is increased roughly by 0.01 eV in almost all the Brillouin zone. In particular, focusing the unoccupied states dominated by 3d orbitals at around 0.09 eV, the eigenvalue tends to behave  $(\varepsilon_{n\mathbf{k}} - \mu) = \varepsilon_{n\mathbf{k}}^0 - \mu_0 + \alpha T^2$ , where  $\varepsilon_{n\mathbf{k}}^0$  and  $\mu_0$  are the eigenvalue and chemical potential, respectively, extrapolated to 0 K, and  $\alpha$  is a positive constant (typical temperature dependence of  $\varepsilon_{n\mathbf{k}} - \mu$  is shown in the inset of Fig. 20). Consequently, the quantity of  $1/(\varepsilon_{n\mathbf{k}} - \mu)$  decreases as temperature, implying a decrease in  $K_b$  considering the second-order perturbation formula for spin-orbit interaction [61]. In the present case, the  $\alpha$  is small so that  $\alpha T^2/(\varepsilon_{n\mathbf{k}}^0 - \mu_0)$  is much smaller than unity, showing a gradual temperature dependence in  $K_b$  like a linear, instead of a complicated dependence. Quantitatively the decreasing rate by the Fermi level smearing should be canceled out partially by the other contributions so as to showing a gradual decline such as observed in the experimental measurement [13].

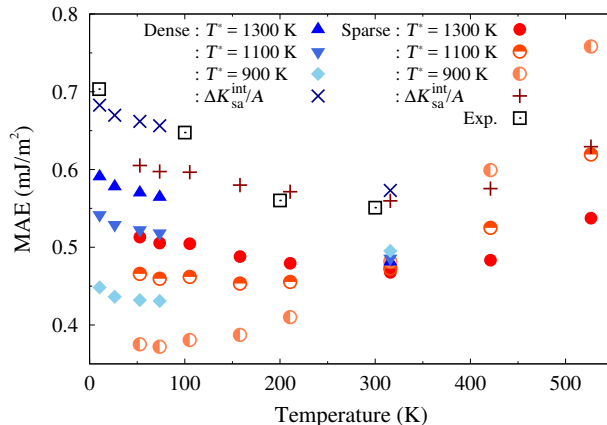


Figure 21: Total magnetic anisotropy energy ( $K$ ) per unit area with respect to temperature. The symbols of triangle, bullet, circle, diamond indicate the data of  $T^* = 900, 1100, 1300\text{K}$  for  $\Delta K_{\text{sa}}^{\text{int}} = 0$  and those of cross and plus for  $T^* = 1300\text{K}$  and  $\Delta K_{\text{sa}}^{\text{int}}/A = 0.09\text{mJ/m}^2$ , where  $A$  is the interface area. The empty square symbols specify the experimental data extracted from reference [13].

### 4.2.3 Including shape magnetic anisotropy

In order to validate the smearing effects obtained above comparing them with the experimental results, we had performed a simulation on  $K$  using the parameters of  $M_0$  and  $T^*$ . In this simulation we used the Fe layer thickness ( $t_{\text{Fe}} = 0.710\text{nm}$ ). This  $t_{\text{Fe}}$  is comparable to those obtained by the first-principles calculation. As a result the  $M_0$  can be fixed to the value which reproduces the experimental magnetization at 300 K ( $M(300\text{K}) = 1.83\text{ T}$ ) [16]. We also found that, comparing the results of the  $T^*$ s of 800, 900, 1000, 1100, 1200, 1300, and 1400K, the  $T^*$ s between 1200K and 1300K give a reasonable fitting to the temperature dependence of available experimental data [13] except a temperature-independent value implying  $\Delta K_{\text{sa}}^{\text{int}}$ . In Fig. 21, the total  $K$  per area are plotted as temperature for the parameters of  $T^* = 900\text{K}, 1100\text{K},$  and  $1300\text{K}$ , where  $\Delta K_{\text{sa}}^{\text{int}} = 0$ . At the lower  $T^*$ s, the in-plane SA becomes larger and the difference with the experimental data also becomes large at the low temperatures.

In Fig. 21, the total  $K$  per unit area is also shown for a non-zero  $\Delta K_{\text{sa}}^{\text{int}}$ . This plot

implies that, assuming the interface contribution of SA ( $\Delta K_{\text{sa}}^{\text{int}}/A = 0.09\text{mJ}/\text{m}^2$ ),  $K$  becomes close to the experimental results. This quantitative assumption in  $\Delta K_{\text{sa}}^{\text{int}}$  is not so far from a realistic contribution, because the quadrupole atomic spin density of prolate type at the interface can reduce the in-plane SA by an energy comparable to that in the free-standing Fe 1ML ( $0.10\text{mJ}/\text{m}^2$ ) [47]. Note that such contribution does not depend on the total magnetization. On the fitting to another experimental data of  $M(300\text{K}) = 2.09\text{T}$ , [50] the set of parameters ( $\Delta K_{\text{sa}}^{\text{int}}/A = 0.35\text{mJ}/\text{m}^2$ ,  $T^* = 1400\text{K}$ ) provides a reasonable temperature dependence in  $K$ . This parameter of  $\Delta K_{\text{sa}}^{\text{int}}$  is not too large, because the parameter originates from both interfaces in the Fe layer. Further investigations on the origin of  $\Delta K_{\text{sa}}^{\text{int}}$  are required for analyzing real magnetic interfaces.

Our analysis in the temperature dependence of  $K$  can predict a behavior at the higher temperatures. As shown in Fig. 21, our result indicates that it increases as temperature after some temperature. Note that such behavior is a consequence that as temperature the perpendicular  $K_{\text{b}}$  decreases and the in-plane SA ( $|K_{\text{sa}}|$ ) also decreases more rapidly with a growth of spin fluctuations. The behavior that the SA works as an enhancement of PMA or as a suppressing origin in the reduction of PMA at higher temperatures, may be one of important general interests in the thin ferromagnetic materials. Note that at further higher temperatures near  $T_{\text{c}}$  the Mermin's approach is no longer useful and should be corrected in accordance with existing large spin-fluctuations [62]. In a further general treatment on magnetic anisotropy, temperature effects originating from a magnetoelastic anisotropy should be considered.

In our analysis, the parameter of  $T^*$  is relatively flexible, compared with the other parameter of  $M_0$ .  $T^*$  around 1300K seems to be suitable to explain the available experimental data. If  $T^*$  is regarded as  $T_{\text{c}}$ , this  $T_{\text{c}}$  ( $= 1300\text{K}$ ) is comparable to those of bcc Fe ( $T_{\text{c}} = 1043\text{K}$ ). When considering a  $T_{\text{c}}$  formula in the approach of localized spin moment,  $T_{\text{c}}$  is proportional to both the exchange coupling constant and the

square of magnetization. Roughly speaking, the effective  $T_c$  may increase, because the magnetic moments on Fe atom tend to be enhanced at the interfaces. Further information on  $T_c$  should be required in the computational approach as well as in the approaches of phenomenological theory and experimental measurement.

Our present approach to a temperature dependent MAE may indicate a correspondence with an available experimental data. However, it is still unclear that the spin fluctuation at finite temperatures is fully considered. This is because that the electronic structure calculation, which is a basis of the MAE originating from the spin-orbit interaction, does not include effects of finite temperature in the atomic spin configuration, whileas the spin configuration at finite temperatures should be an ensemble of various directions for atomic magnetic moments. The last picture is a reason why the strength of total magnetization tends to decrease as temperature. An improved approach on MAE estimation is required for a computational material design of magnetic materials.

## 4.2.4 The change of density of states

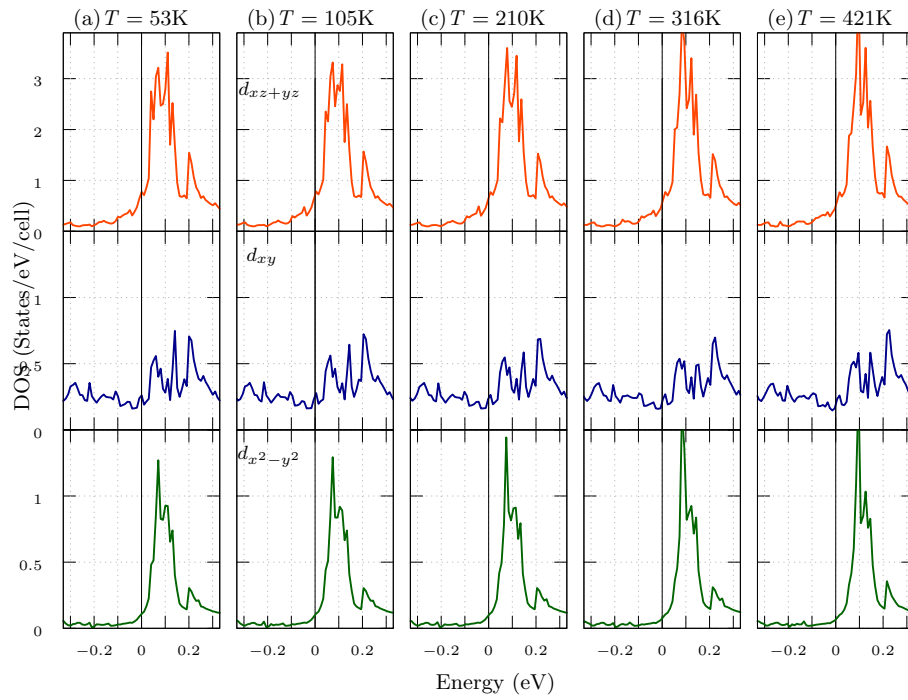


Figure 22: Temperature dependence on the Density of states of Cr6/Fe5/MgO5 system

When we increase the temperature the interface resonant state are change, its become more sharp and closer to the Fermi level. This feature support the phenomena of higher perpendicular magnetic anisotropy energy.

## 5 Conclusion and Future Works

### 5.1 Conclusion

Systematic investigation on Cr-buffered Fe/MgO interface has been performed in this work. Starting from the change in thickness of ferromagnet layer, until the temperature dependence by the change of Fermi level smearing. We performed first principles electronic structure calculations for the interface systems with Cr under-layer of Fe/MgO interface and estimated the MAE originating from the SOI and MDI. The exotic oscillating behavior was observed in the MAE from SOI. We found that the DFT approach can describe the MAE with good accuracy, compared with the experimental data. Our calculation shows that the MAE(SOI) in 5ML system with  $1.5 \text{ mJ/m}^2$  is comparable to the experimental ones. The series of total MAE's indicated perpendicular and in-plane magnetic anisotropies in the Cr-underlayer Fe/MgO. The reduction by the in-plane shape anisotropy energy was considered as the correction factor to the pure DFT calculation approach. By introducing the rescaled magnetization similar to the experimental one, the thickness range of perpendicular magnetic anisotropy was found to correspond to experimental result. From the electronic structure, the dispersionless and saddle point nature appear in the band dispersions around  $\mathbf{k}_1$  are found to play the important role in the perpendicular anisotropy. In the Fe 2ML, particularly, the flat bands consisting of  $d_{xz}$ ,  $d_{yz}$ ,  $d_{xy}$ ,  $d_{x^2-y^2}$  are located just below and above the Fermi level. These bands contribute to the large MAE(SOI) of  $2 \text{ mJ/m}^2$ . The change of interface states as an effect of vicinity of Cr under-layer and the formation of quantum-well is discussed as the origin of change in perpendicular magnetic anisotropy like a proximity effect. The detail electronic and magnetic properties of this Cr buffered Fe/MgO slab systems,

might be useful in future materials design for such multi-functional interfaces.

Based on similar first-principles calculation method, the MAE from the band energy contribution using the temperature-dependent Fermi level smearing in the Fe(5ML)/MgO slab was considered. The contribution of the MAE decreases by 0.4 mJ/m<sup>2</sup> as temperature from 10.5K to 527K. When employing the simple formula for the SA and assuming the experimental saturated magnetization with the appropriate temperature dependence for ultra-thin films, the total MAE shows a nearly flat part around the room temperature. This theoretical analysis may predict an increase of the perpendicular total MAE at higher temperatures. Such increase may be a possible general consequence of the balance between a large perpendicular band energy contribution and small in-plane shape anisotropy. The present work provides a new pathway to understand origins of a temperature dependence in MAE.

## 5.2 Future Works

Details of sign change in electric field effect in 2 ML configuration of the Cr(6)/Fe(*x*)/MgO(5) system need to be discussed in future, considering large change in magnitude of 123 fJ/Vm electric field effect coefficient. The details on the electric field effect from the smearing effect also planned to be reported in future works.

## A Appendix

### A.1 Thickness dependence of MAE and its EF effect

One of the target in this research is to find material with large perpendicular magnetic anisotropy energy and also responsive to the voltage change, which is have large electric field effect coefficient. Motivated by the search for better material, we try by varying the thickness of ferromagnet. In hope this work will provide better understanding of the underlying mechanism of PMA and EFE.

#### A.1.1 Cr(6)/Fe(1)/MgO(5)

In this work we start to build our model by begin to calculate from single monolayer of iron. With single layer of ferromagnet we try to investigate the electronic structure, atomic structure, and finally observe the EFE and MAE.

##### A.1.1.1 Optimized Structure

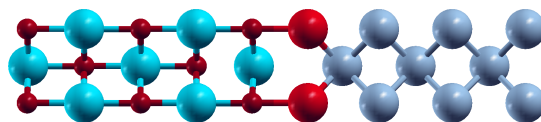


Figure 23: The atomic structure model in Cr(6)/Fe(1)/MgO(5)

We optimize the structure of this material, as described in Fig. 23. The most important part of this structure is optimized distance, the optimized interface distance of this material are 2.18 Angstrom.

### A.1.1.2 Electronic Structure

The electronic structure of interface atom play important role in determining the magnetic anisotropy energy and its electric field effect characteristic.

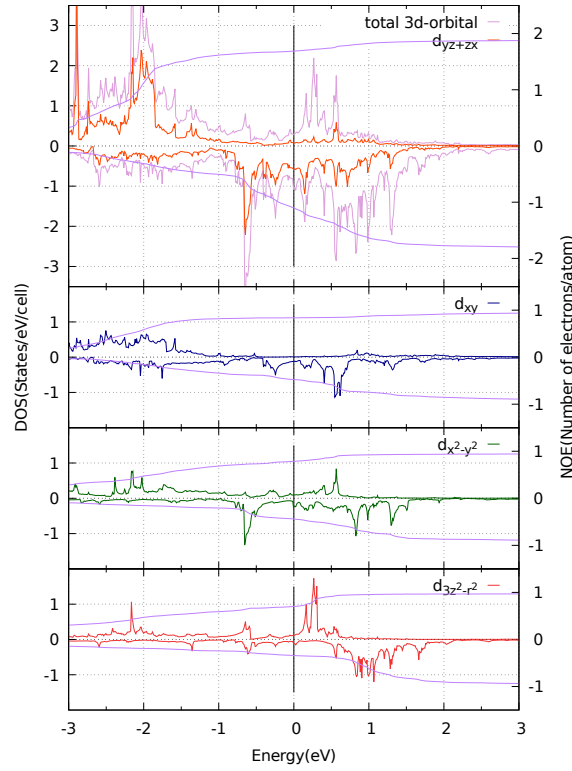


Figure 24: The density of states of Cr(6)/Fe(1)/MgO(5)

We can see here, from the density of states of 1 monolayer of iron configuration in Fig. 24 that we could see there is some states of majority spin in the unoccupied states, especially comes from  $3z^2-r^2$ . we could also see the 3d  $xy$  and  $yz$  orbital states are available at Fermi level. It seems like this iron are much likely interfered by underlying chromium. From the band dispersion its more clear that we can observe there is a lot of states of the  $3z^2-r^2$  near Fermi level, especially from 1eV to below. Also we could observed that  $yz$  and  $zx$  band at the  $\Gamma$  point are exactly at the Fermi level.

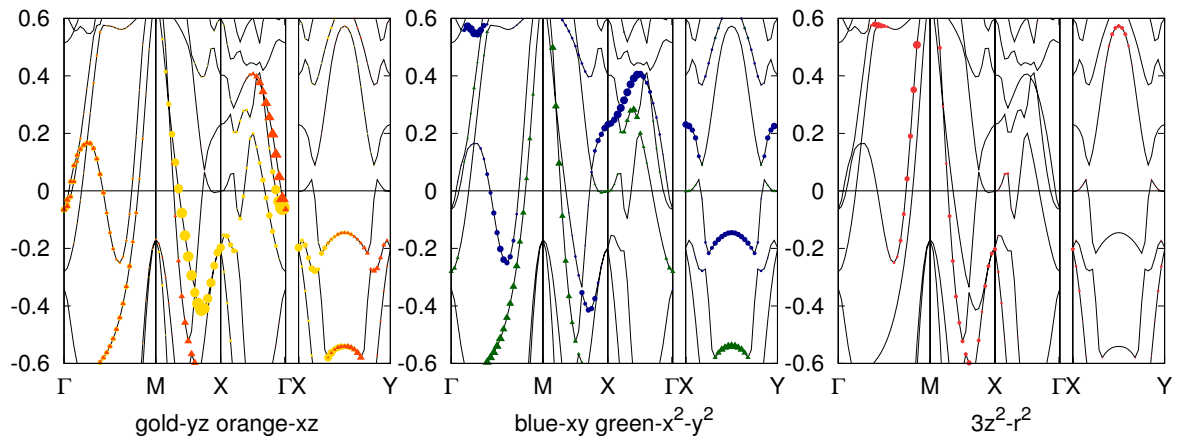


Figure 25: The band dispersion of Cr(6)/Fe(1)/MgO(5)

### A.1.1.3 Magnetic Anisotropy Energy and Electric Field Effect

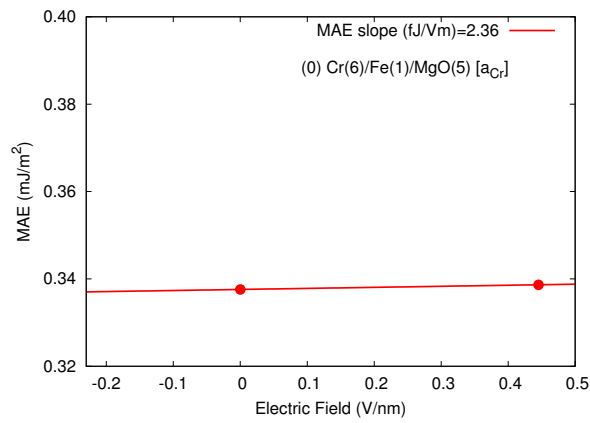


Figure 26: Electric field effect in Cr(6)/Fe(1)/MgO(5)

## A.1.2 Cr(6)/Fe(2)/MgO(5)

### A.1.2.1 Optimized Structure

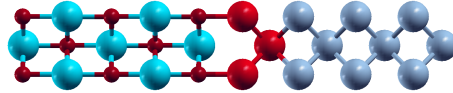


Figure 27: The atomic structure model in Cr(6)/Fe(2)/MgO(5)

We optimize the structure of this material, as described at 27. The optimized interface distance for this structure is 2.20 Angstrom.

### A.1.2.2 Electronic Structure

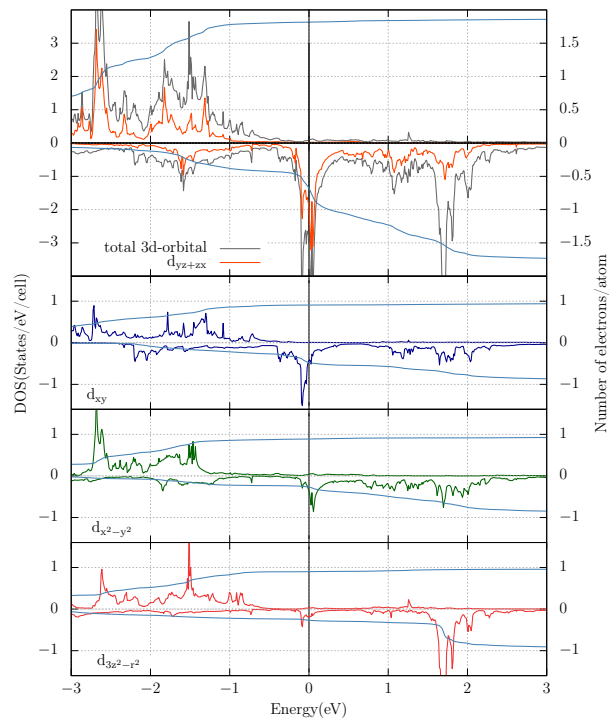


Figure 28: The density of states of Cr(6)/Fe(2)/MgO(5)

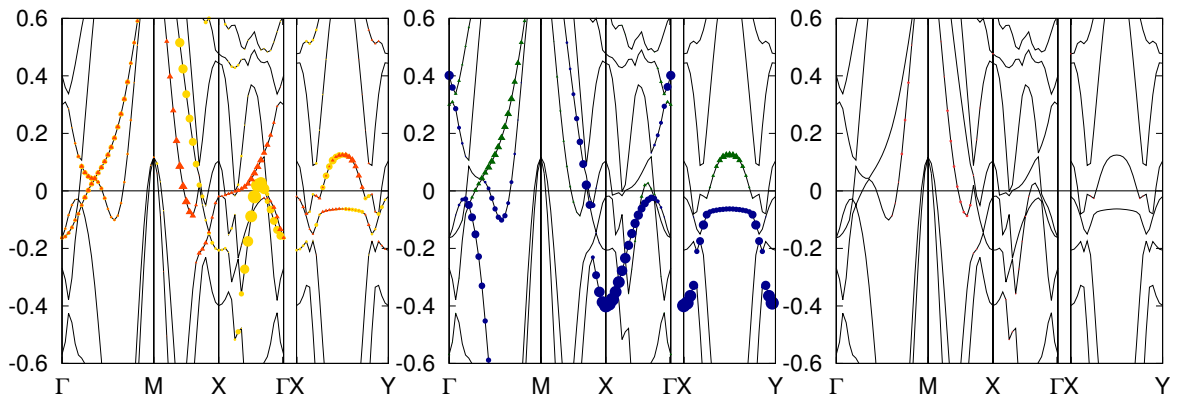


Figure 29: The band dispersion of Cr(6)/Fe(2)/MgO(5)

Two monolayer configuration give the highest value of magnetic anisotropy energy from the spin orbit coupling contribution. The main difference could be notified from the 1 monolayer configuration is the formation of sharp peak just above Fermi level at the minority unoccupied states of the 3d orbitals. We call this peak the interface resonant states, because its correlated with the IRS observed in experiment. The observation from band dispersion in Fig. 29 show clear demonstration of band splitting of the  $xz$  and  $yz$  orbital at  $\Gamma$  point of the Fermi Level, the band energy split in to above and below Fermi level. Here we also could observe that  $x^2 - r^2$  orbital are pushed away from the Fermi level.

### A.1.2.3 Magnetic Anisotropy Energy and Electric Field Effect

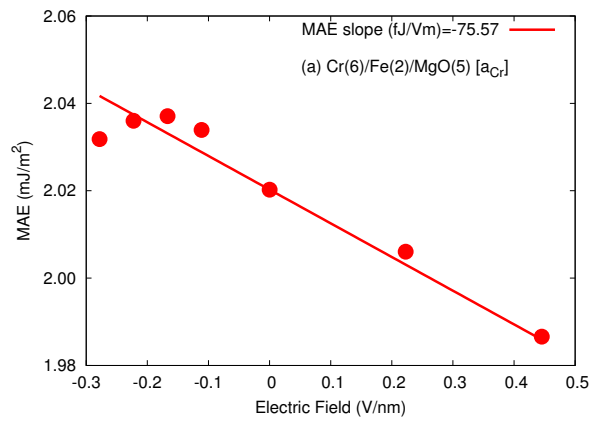


Figure 30: Electric field effect in Cr(6)/Fe(2)/MgO(5)

### A.1.3 Cr(6)/Fe(3)/MgO(5)

#### A.1.3.1 Optimized Structure

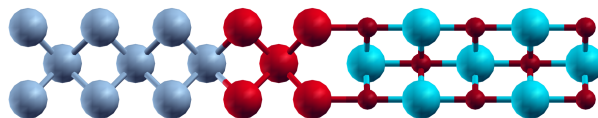


Figure 31: The atomic structure model in Cr(6)/Fe(3)/MgO(5)

We optimize the structure of this material, as described at 31. Optimized distance for this structure is 2.20 Angstrom.

A.1.3.2 Electronic Structure

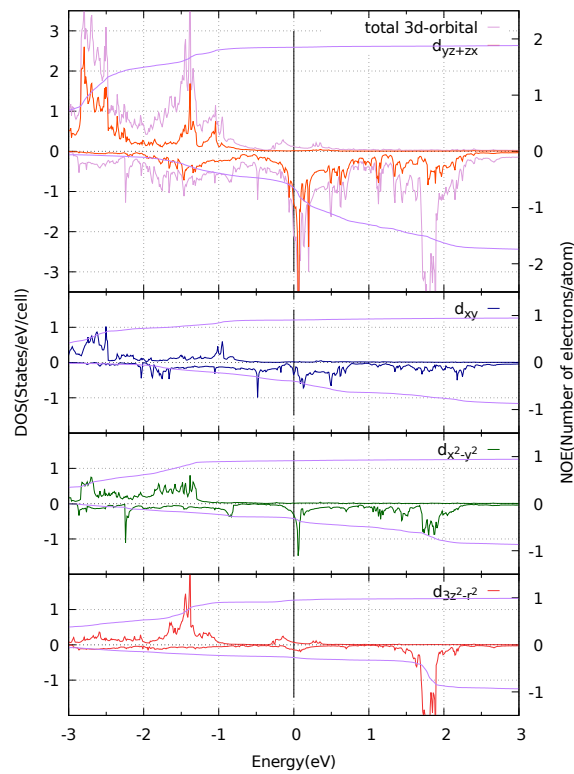


Figure 32: The density of states of Cr(6)/Fe(3)/MgO(5)

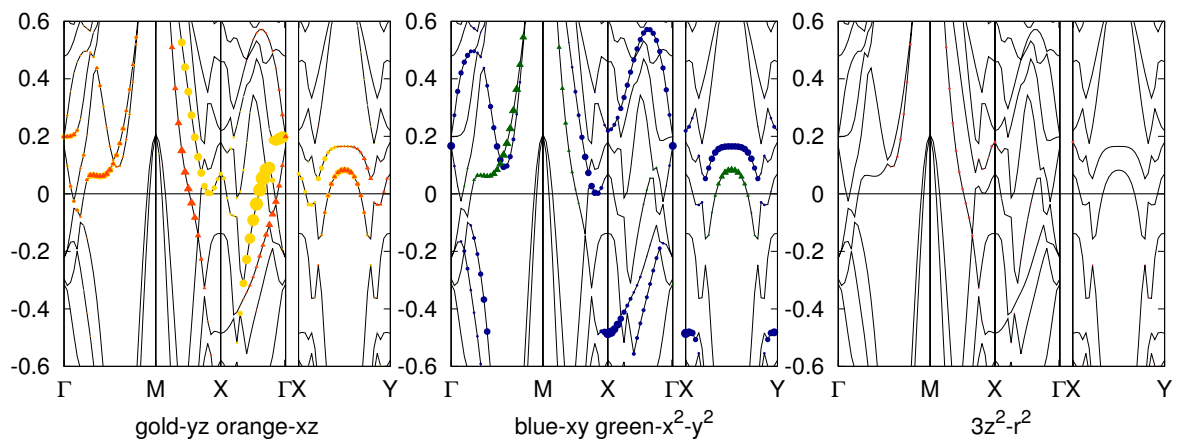


Figure 33: The band dispersion of Cr(6)/Fe(3)/MgO(5)

### A.1.3.3 Magnetic Anisotropy Energy and Electric Field Effect

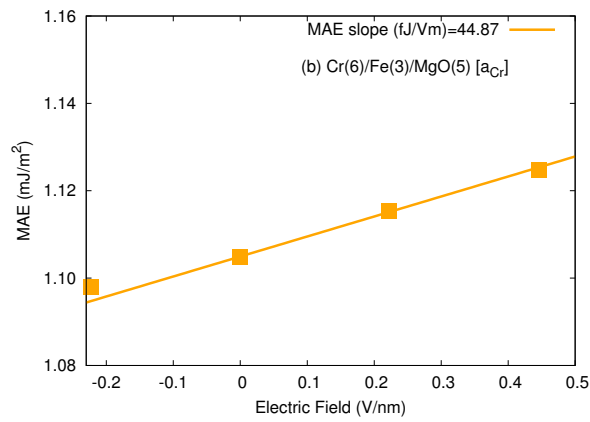


Figure 34: Electric field effect in Cr(6)/Fe(3)/MgO(5)

### A.1.4 Cr(6)/Fe(4)/MgO(5)

#### A.1.4.1 Optimized Structure



Figure 35: The atomic structure model in Cr(6)/Fe(4)/MgO(5)

We optimize the structure of this material, as described at 35. Optimized distance of this structure is 2.21 Angstrom.

A.1.4.2 Electronic Structure

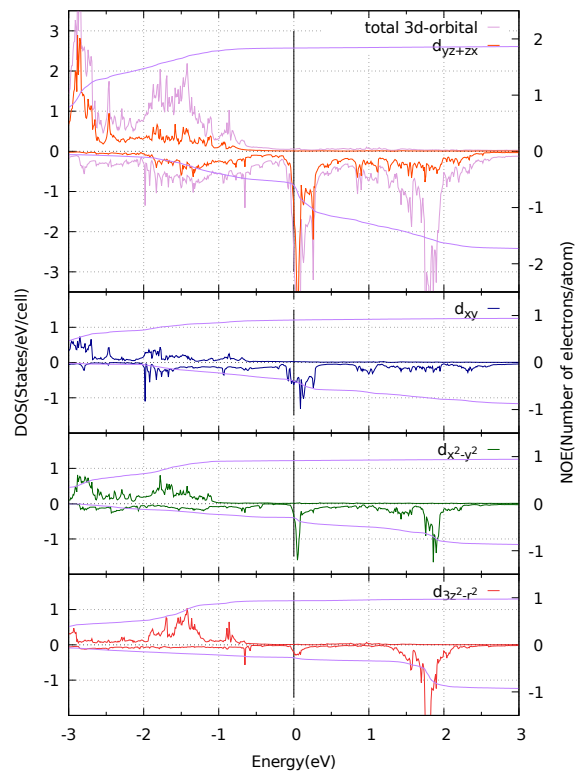


Figure 36: The density of states of Cr(6)/Fe(4)/MgO(5)

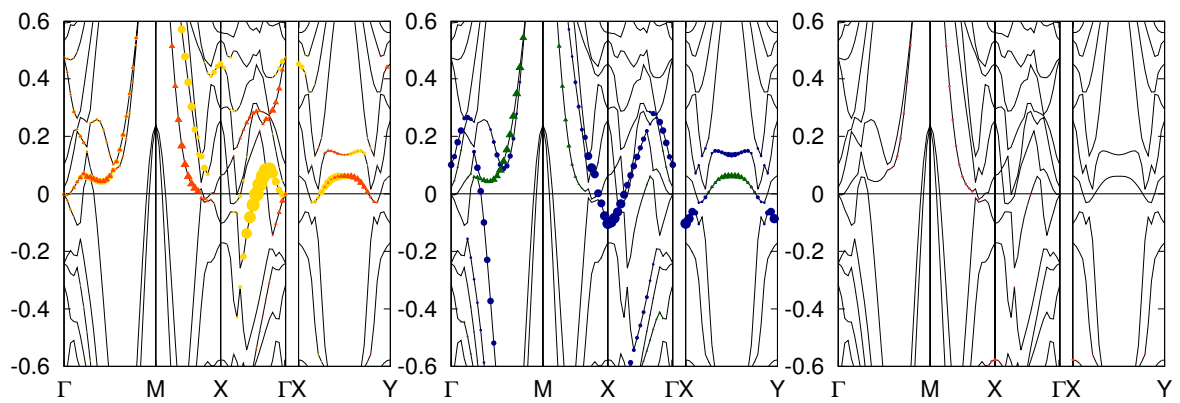


Figure 37: The band dispersion of Cr(6)/Fe(4)/MgO(5)

### A.1.4.3 Magnetic Anisotropy Energy and Electric Field Effect

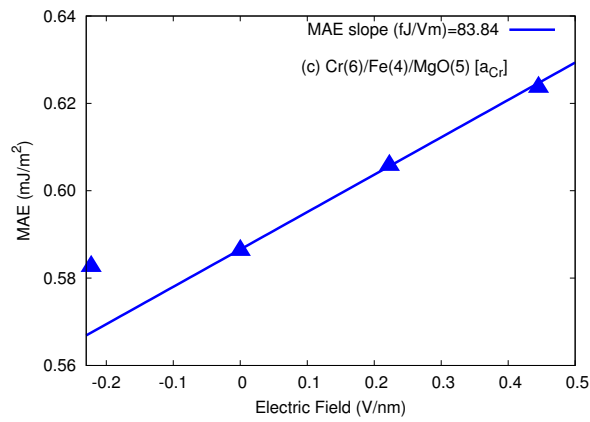


Figure 38: Electric field effect in Cr(6)/Fe(4)/MgO(5)

### A.1.5 Cr(6)/Fe(5)/MgO(5)

#### A.1.5.1 Optimized Structure



Figure 39: The atomic structure model in Cr(6)/Fe(5)/MgO(5)

We optimize the structure of this material, as described at 39. Optimized interface distance for this structure is 2.22 Angstrom.

## A.1.5.2 Electronic Structure

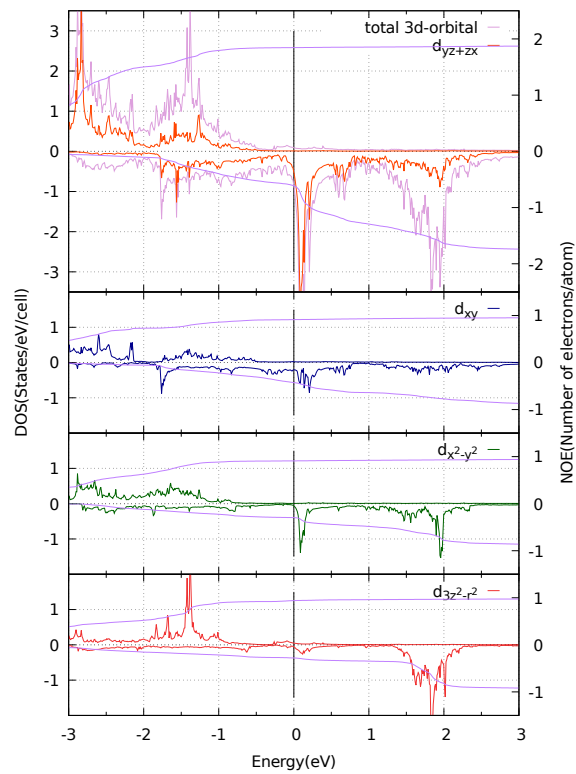


Figure 40: The density of states of Cr(6)/Fe(5)/MgO(5)

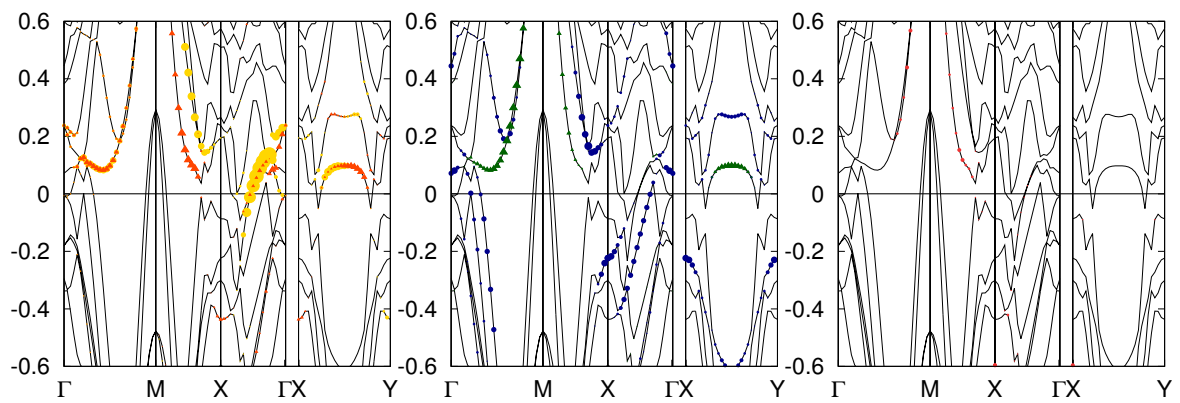


Figure 41: The band dispersion of Cr(6)/Fe(5)/MgO(5)

### A.1.5.3 Magnetic Anisotropy Energy and Electric Field Effect

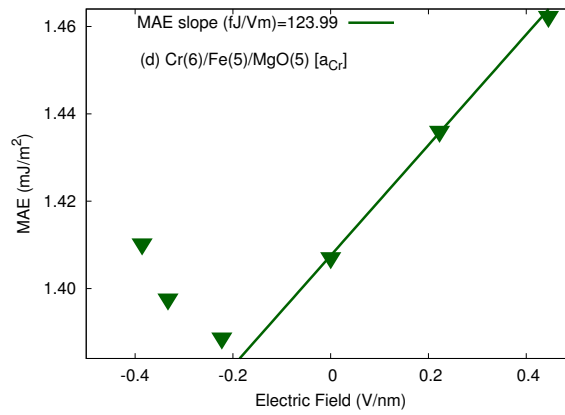


Figure 42: Electric field effect in Cr(6)/Fe(5)/MgO(5)

### A.1.6 Cr(6)/Fe(6)/MgO(5)

#### A.1.6.1 Optimized Structure



Figure 43: The atomic structure model in Cr(6)/Fe(6)/MgO(5)

We optimize the structure of this material, as described at 43. Optimized interface distance for this structure is 2.21 Angstrom.

A.1.6.2 Electronic Structure

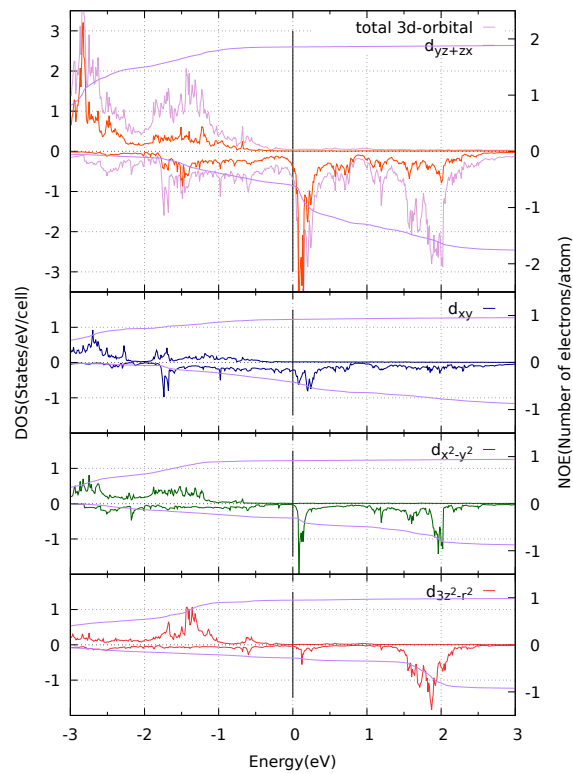


Figure 44: The density of states of Cr(6)/Fe(6)/MgO(5)

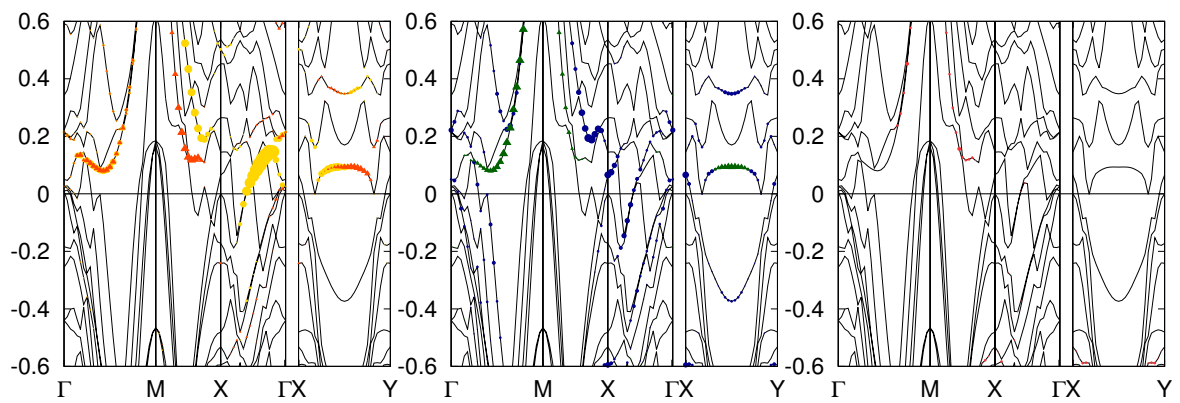


Figure 45: The band dispersion of Cr(6)/Fe(6)/MgO(5)

### A.1.6.3 Magnetic Anisotropy Energy and Electric Field Effect

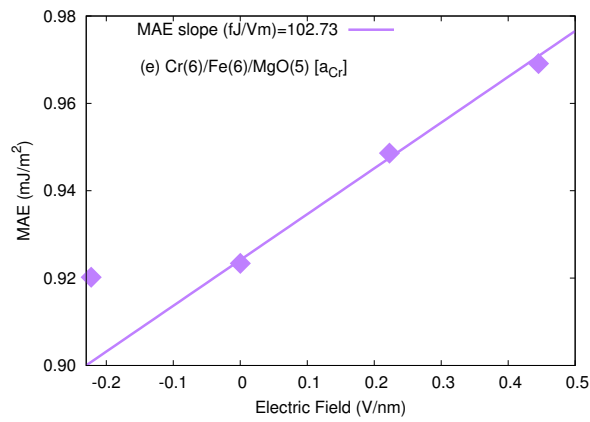


Figure 46: Electric field effect in Cr(6)/Fe(6)/MgO(5)

### A.1.7 Cr(6)/Fe(7)/MgO(5)

#### A.1.7.1 Optimized Structure



Figure 47: The atomic structure model in Cr(6)/Fe(7)/MgO(5)

We optimize the structure of this material, as described at 47. Optimized interface distance for this structure is 2.21 Angstrom.

A.1.7.2 Electronic Structure

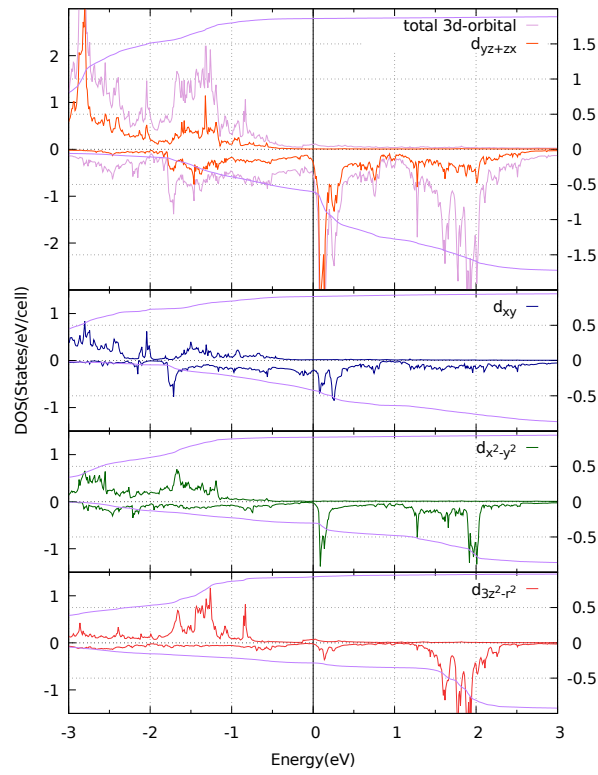


Figure 48: The density of states of Cr(6)/Fe(7)/MgO(5)

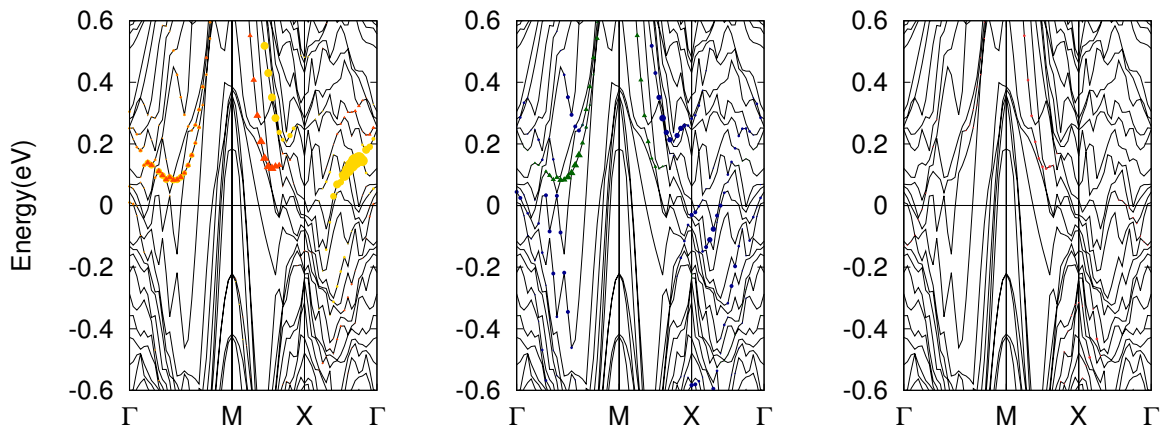


Figure 49: The band dispersion of Cr(6)/Fe(7)/MgO(5)

### A.1.7.3 Magnetic Anisotropy Energy and Electric Field Effect

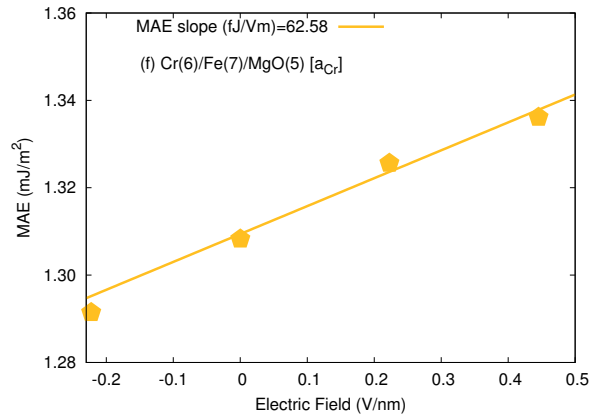


Figure 50: Electric field effect in Cr(6)/Fe(7)/MgO(5)

### A.1.8 Cr(6)/Fe(8)/MgO(5)

#### A.1.8.1 Optimized Structure

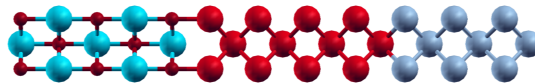


Figure 51: The atomic structure model in Cr(6)/Fe(8)/MgO(5)

We optimize the structure of this material, as described at 51. Optimized interface distance for this structure is Angstrom.

A.1.8.2 Electronic Structure

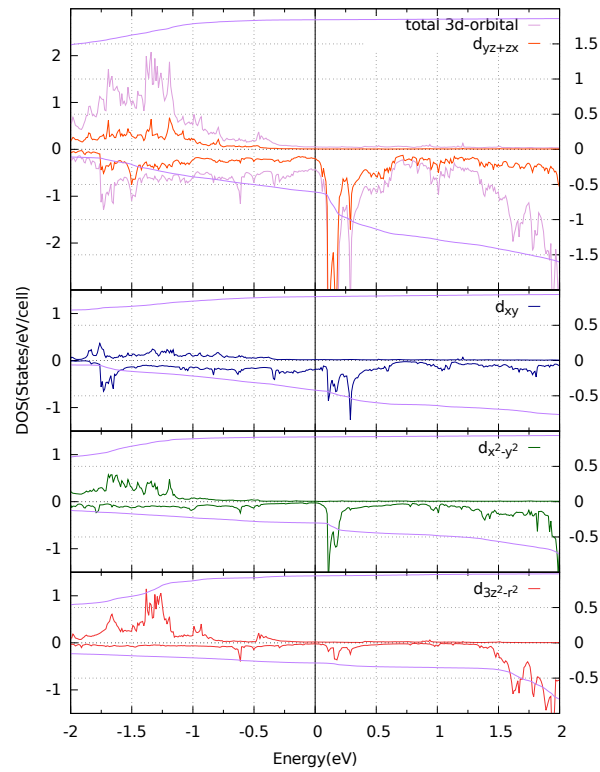


Figure 52: The density of states of Cr(6)/Fe(8)/MgO(5)

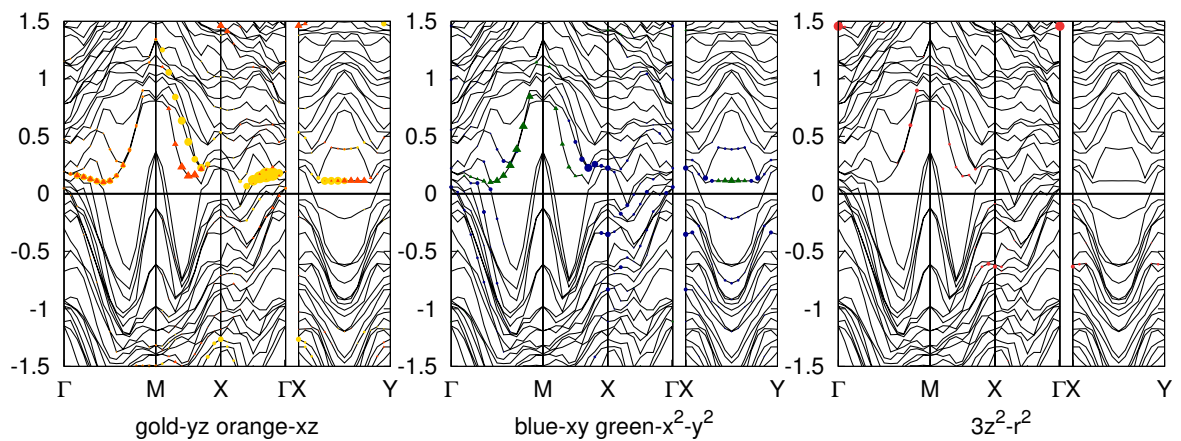


Figure 53: The band dispersion of Cr(6)/Fe(8)/MgO(5)

### A.1.8.3 Magnetic Anisotropy Energy and Electric Field Effect

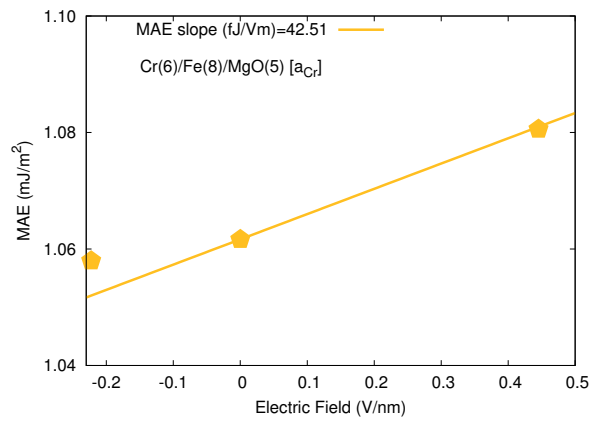


Figure 54: Electric field effect in Cr(6)/Fe(8)/MgO(5)

### A.1.9 Cr(6)/Fe(9)/MgO(5)

#### A.1.9.1 Optimized Structure

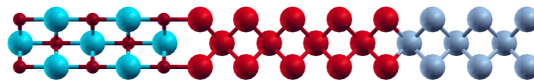


Figure 55: The atomic structure model in Cr(6)/Fe(9)/MgO(5)

We optimize the structure of this material, as described at 55. Optimized interface distance for this structure is Angstrom.

A.1.9.2 Electronic Structure

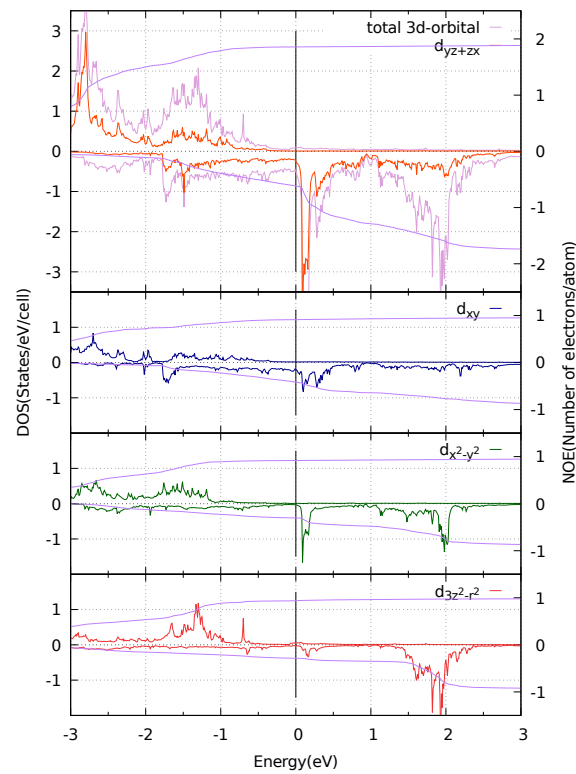


Figure 56: The density of states of Cr(6)/Fe(9)/MgO(5)

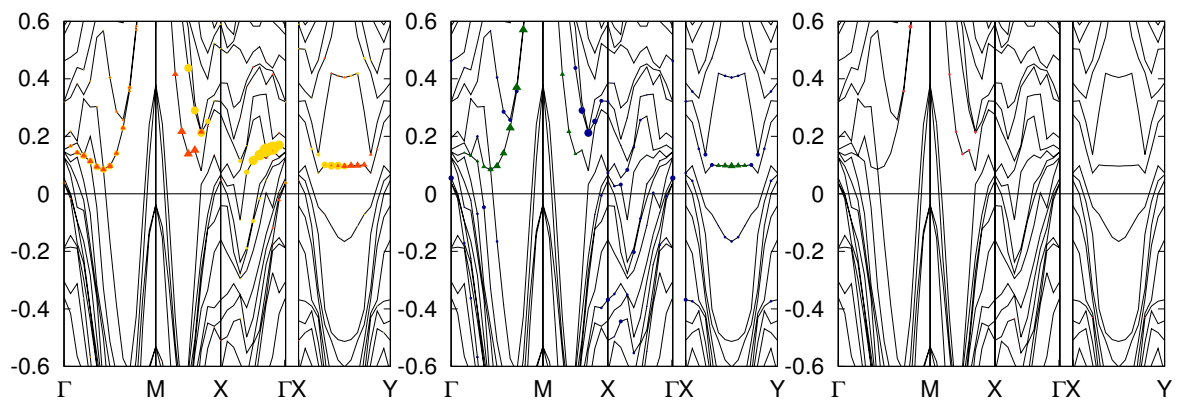


Figure 57: The band dispersion of Cr(6)/Fe(9)/MgO(5)

### A.1.9.3 Magnetic Anisotropy Energy and Electric Field Effect

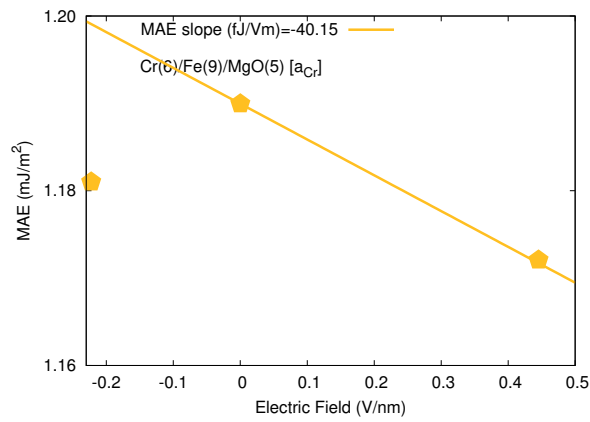


Figure 58: Electric field effect in Cr(6)/Fe(9)/MgO(5)

### A.1.10 Cr(6)/Fe(10)/MgO(5)

#### A.1.10.1 Optimized Structure



Figure 59: The atomic structure model in Cr(6)/Fe(10)/MgO(5)

We optimize the structure of this material, as described at 59. Optimized interface distance for this structure is Angstrom.

A.1.10.2 Electronic Structure

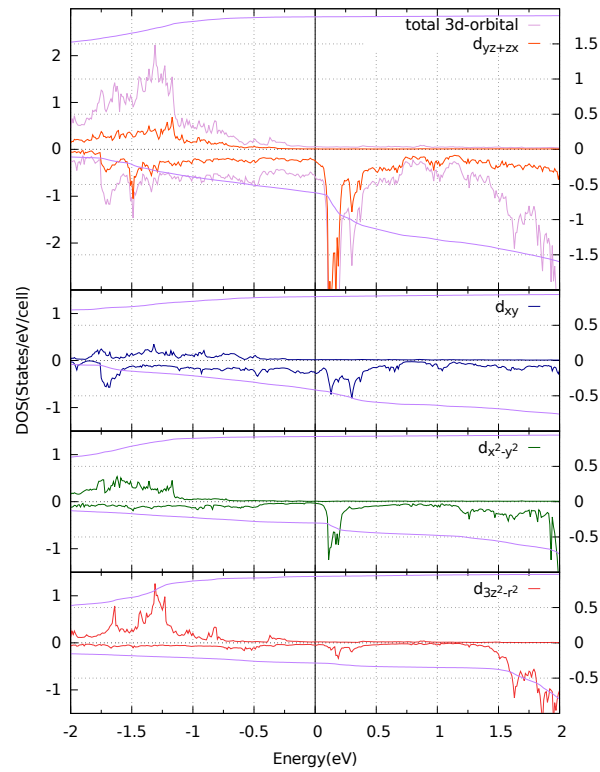


Figure 60: The density of states of Cr(6)/Fe(10)/MgO(5)

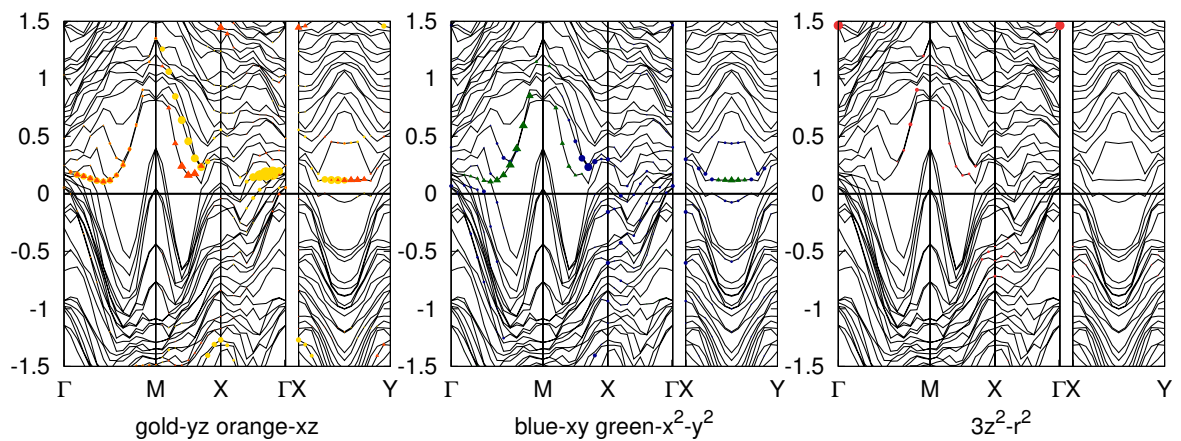


Figure 61: The band dispersion of Cr(6)/Fe(10)/MgO(5)

## A.2 Co Dopping to the Fe(3)/MgO(3) interface

In this part we report the effect of Co impurity to Fe/MgO interface. Most of the tunnel junction or also known as spin valve device are based on FeCoB for the magnetic thin film element. This material chosen because the economy of fabrication process, one can synthesize the crystal from the amorphous state, then the thin film crystallize during the annealing process. During the annealing, Boron (B) are oxidized and disappear from the system, leaving Co-doped Fe/MgO interface. It still not clear for us the effect of Co in the ferromagnetic thin layer, therefore we perform first principles simulation to understand the impurity effect on this interface.

### A.2.1 Type A insertion

In this configuration we inserted the cobalt at the interface.

#### A.2.1.1 Optimized Structure

The model of 3ML of MgO and 3 ML of ferromagnet was taken into consideration

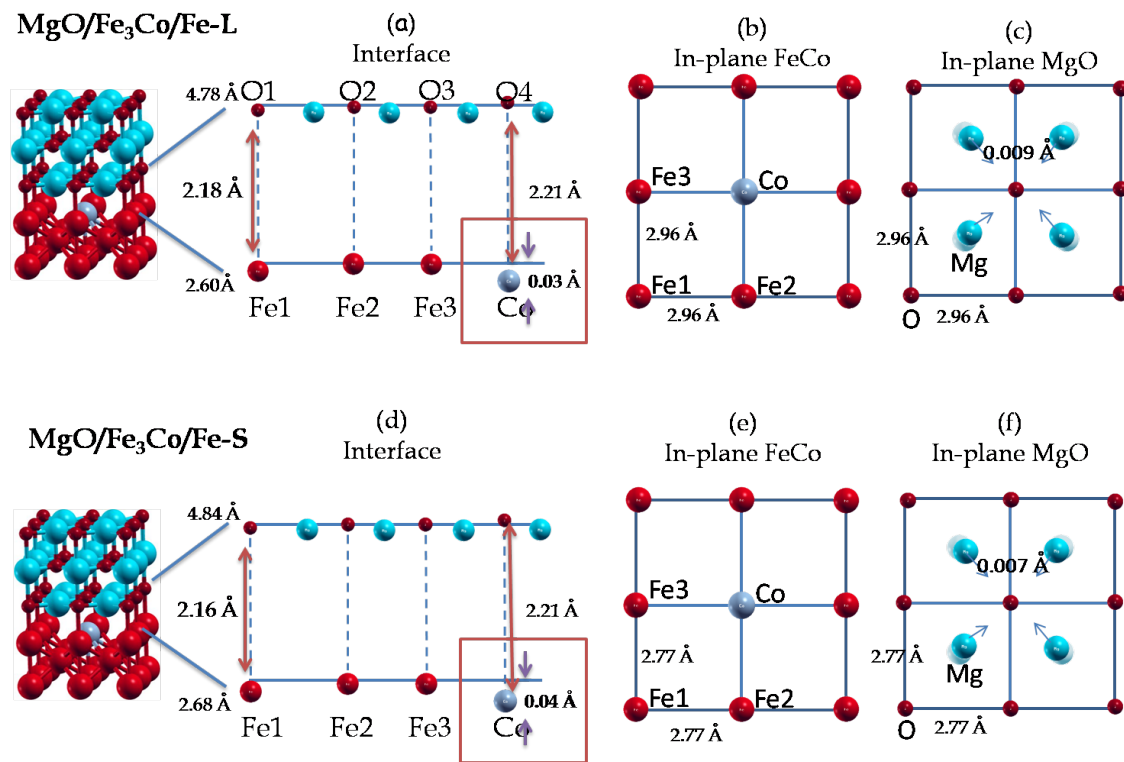


Figure 62: The optimized structure of Fe(2)/Fe(1 - x)Co(x)/MgO(3)

## A.2.1.2 Electronic Structure

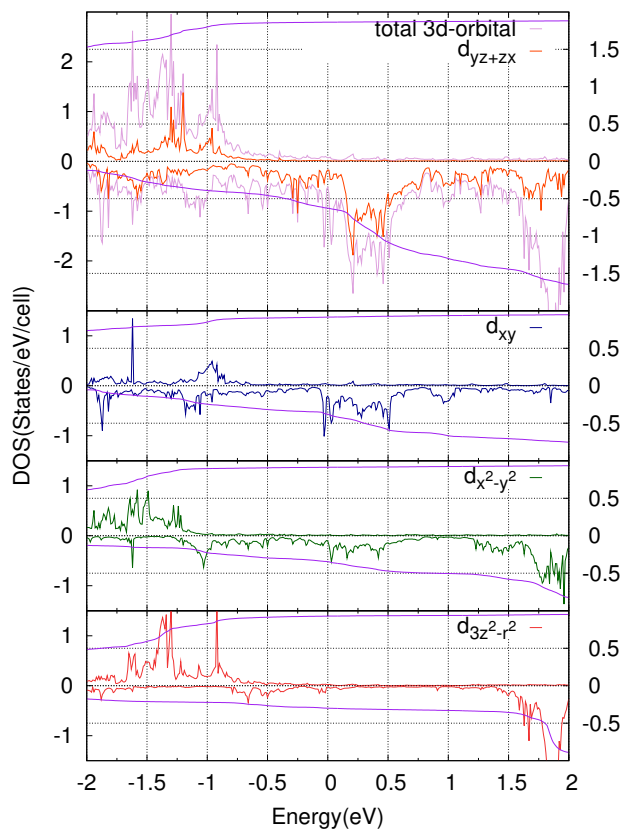


Figure 63: The density of states of iron in Fe(2)/Fe(1 - x)Co(x)/MgO(3)

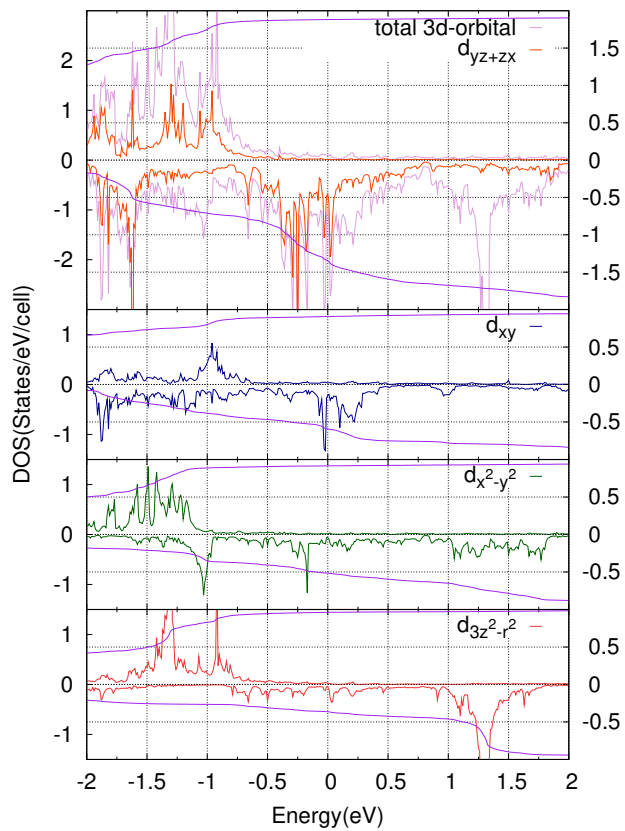


Figure 64: The density of states of cobalt in Fe(2)/Fe(1 - x)Co(x)/MgO(3)

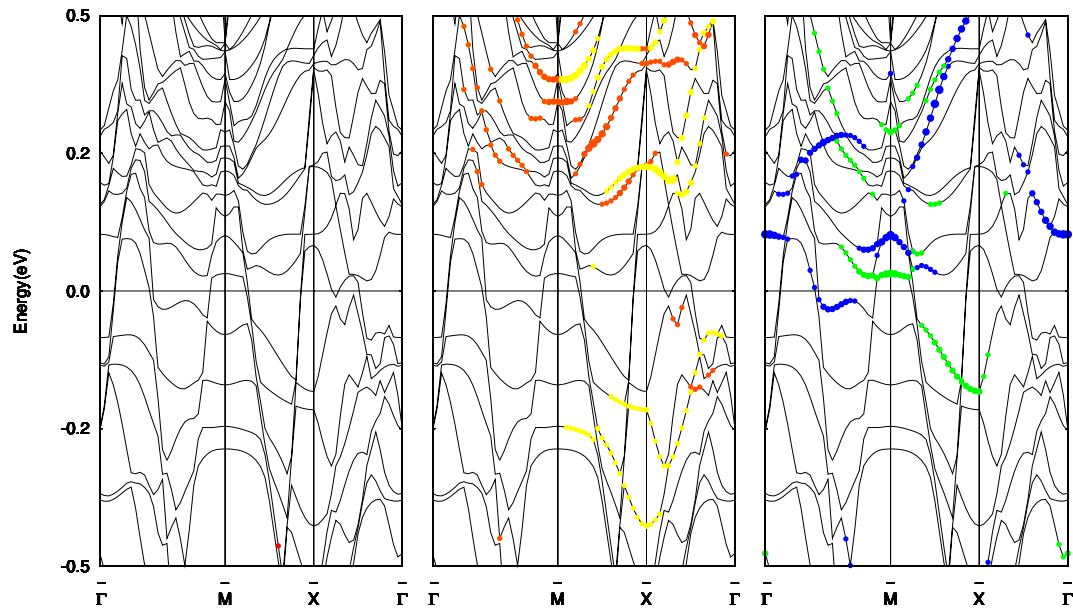


Figure 65: The band dispersion of Fe(2)/Fe(1 -  $x$ )Co( $x$ )/MgO(3)

## A.2.2 Type B insertion

In this configuration we inserted the cobalt at the middle layer of ferromagnet.

### A.2.2.1 Optimized Structure

The model of 3ML of MgO and 3 ML of ferromagnet was taken into consideration

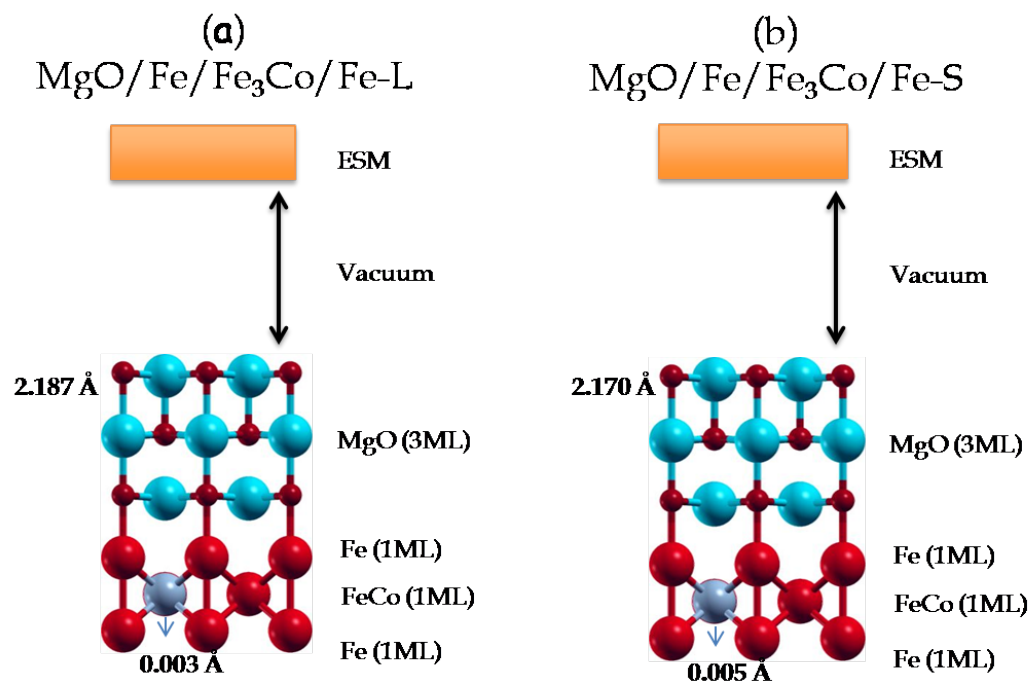


Figure 66: The optimized structure of Fe/Fe(1 - x)Co(x)/Fe/MgO(3)

## A.2.2.2 Electronic Structure

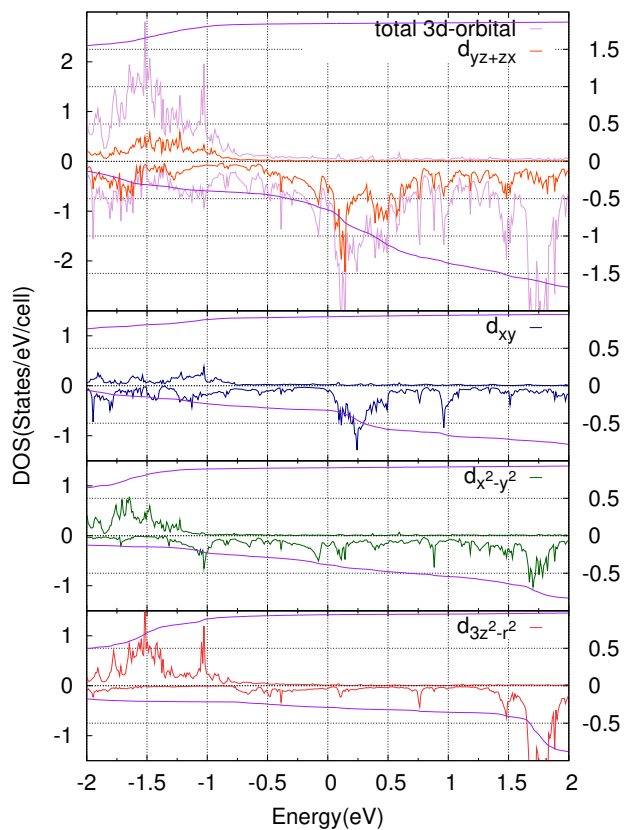


Figure 67: The density of states of iron in Fe/Fe(1 - x)Co(x)/Fe/MgO(3)

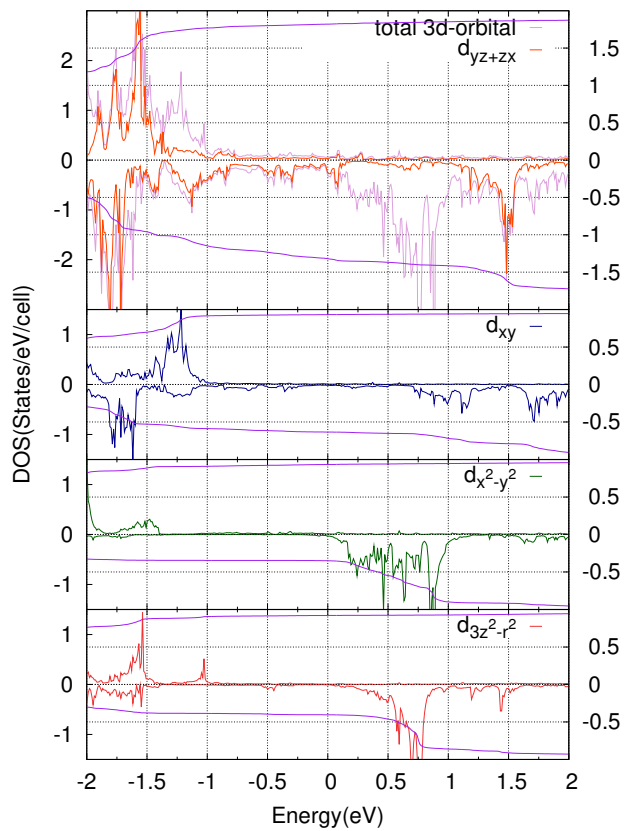


Figure 68: The density of states of cobalt in Fe/Fe(1 - x)Co(x)/Fe/MgO(3)

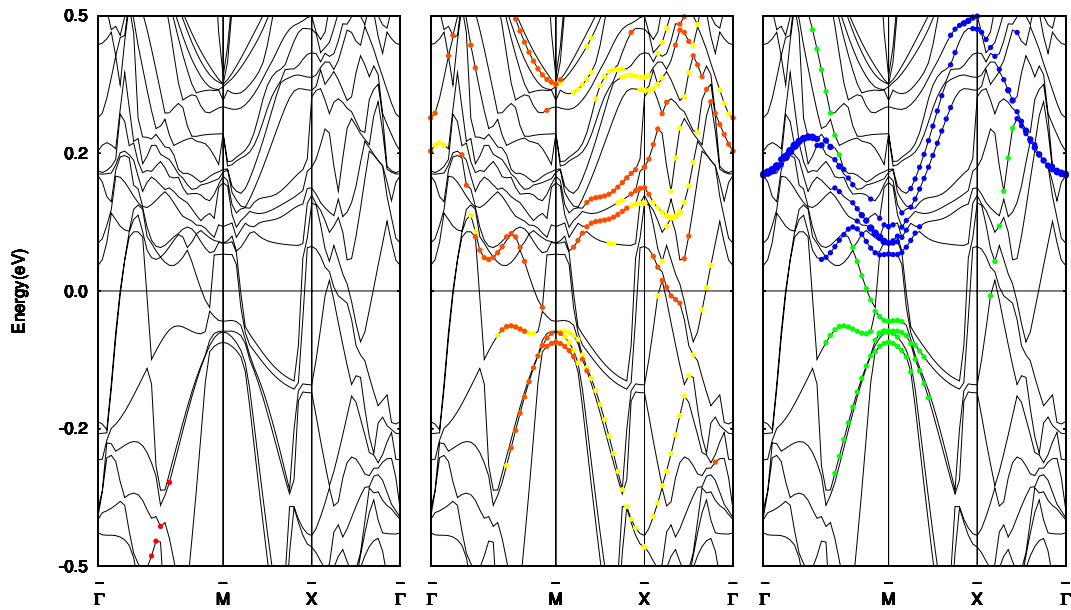


Figure 69: The band dispersion of Fe/Fe(1 - x)Co(x)/Fe/MgO(3)

### A.2.3 Comparative study on Magnetic Anisotropy Energy and Electric Field Effect

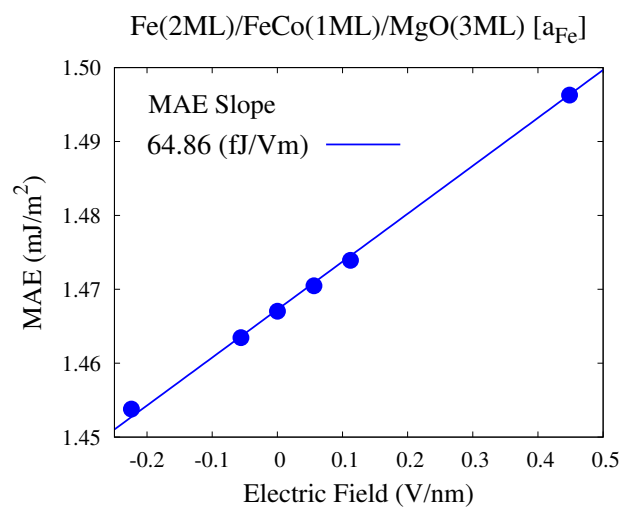


Figure 70: The electric field effect of Fe(2)/Fe(1 - x)Co(x)/MgO(3)

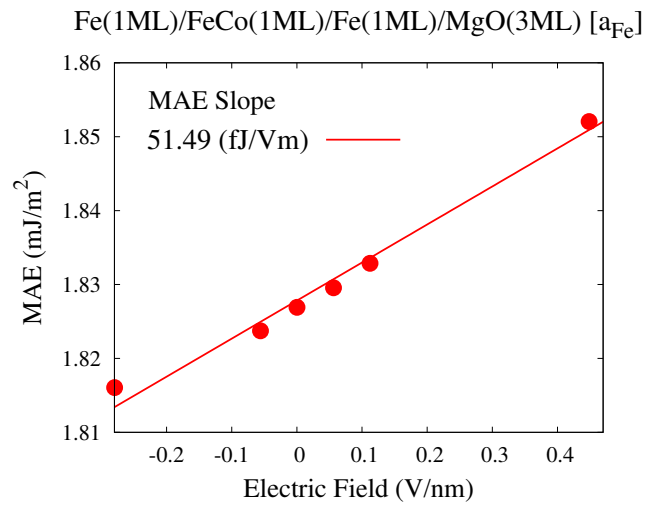


Figure 71: The electric field effect of Fe/Fe(1 - x)Co(x)/Fe/MgO(3)

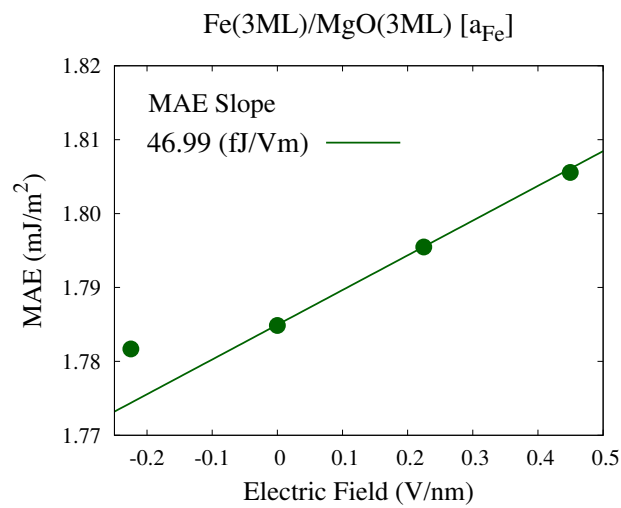


Figure 72: The electric field effect of Fe(3)/MgO(3)

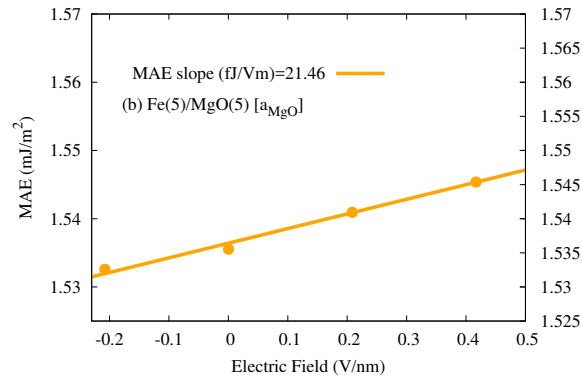


Figure 73: The electric field effect of Fe(5)/MgO(5)

From the comparative study we found that Co impurity enhance both PMA and EFE when its located in the nearest neighbor layer to the Fe/MgO interface. More significant increase of EFE can be observed when we introduce impurity at the interface, this configuration change the shape and peak location of resonance states of interface iron. But in type-a configuration PMA are decreased when compared to the pure Fe/MgO interface.

## A.3 Different underlayer effect

### A.3.1 W underlayer

Tungsten buffer layer proposed in this works because it was found that W could increase the thermal stability of Fe/MgO interface during annealing temperature. It has been known that FeCoB/MgO has low thermal stability due to rapid decrease of PMA during annealing process over 300K.

#### A.3.1.1 Optimized Structure

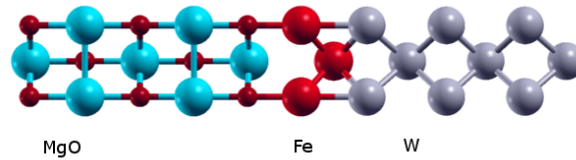


Figure 74: Structure of W(6)/Fe(2)/MgO(5) system

## A.3.1.2 Electronic Structure

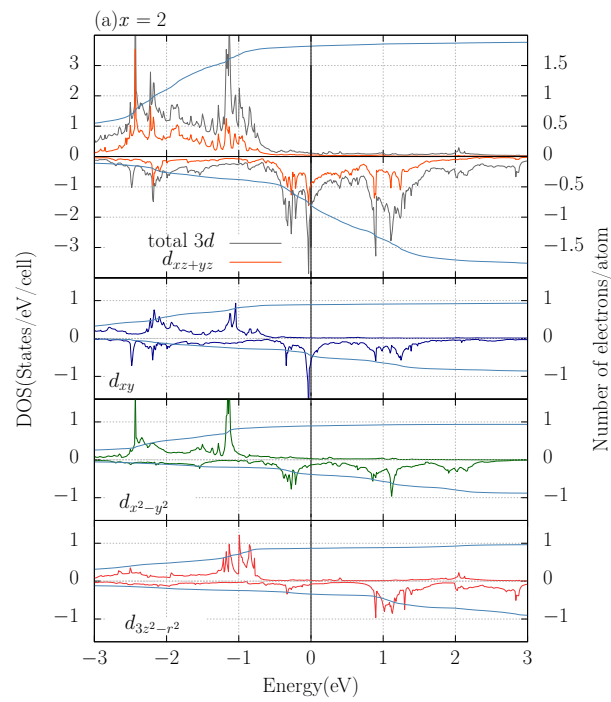


Figure 75: Density of states of the W(6)/Fe(2)/MgO(5) system

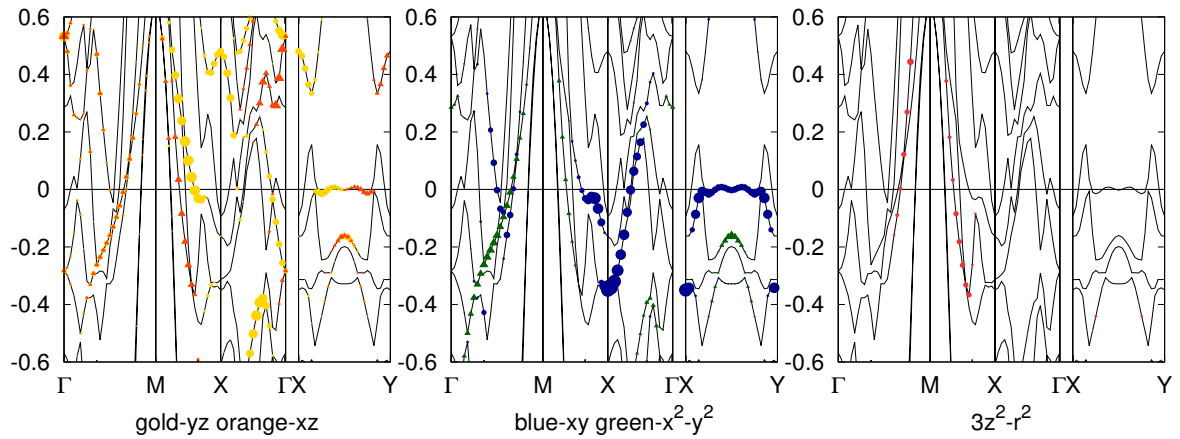


Figure 76: Band dispersion of W(6)/Fe(2)/MgO(5) system

## A.4 Magnetic moments of density functional approach

The magnetic moments obtained by the density functional approach are displayed for typical temperatures of 53K (sparse mesh) and 316K (sparse mesh) in Table 1 and Table 2. These data were estimated from the spin density by integrating it in the atomic sphere with the radius (Fe: 1.32Å, Cr: 0.90Å).

Table 1: Spin magnetic moments in  $\mu_B$  on Cr and Fe atoms. The temperature specifies the value used in the Fermi level smearing. [001]( $z$ -direction) and [100]( $x$ -direction) specify the direction of total magnetization.

Temperature	Total	Fe(1)	Fe(2)	Fe(3)	Fe(4)	Fe(5)
53K [001]	12.7964	2.8481	2.5311	2.5984	2.4986	2.3202
53K [100]	12.7964	2.8499	2.5295	2.5975	2.4992	2.3203
316K [001]	12.7844	2.8420	2.5286	2.5960	2.5008	2.3170
316K [100]	12.7848	2.8428	2.5286	2.5957	2.5007	2.3170
Temperature	Cr(1)	Cr(2)	Cr(3)	Cr(4)	Cr(5)	Cr(6)
53K [001]	-1.0678	0.9999	-1.0902	1.2247	-1.4434	2.3329
53K [100]	-1.0674	0.9999	-1.0903	1.2245	-1.4433	2.3330
316K [001]	-1.0689	0.999	-1.0905	1.2209	-1.4421	2.3309
316K [100]	-1.0689	0.9989	-1.0906	1.2208	-1.4421	2.3308

Table 2: Orbital magnetic moments in  $\mu_B$  on Cr and Fe atoms. The temperature specifies the value used in the Fermi level smearing.

Temperature	Total	Fe(1)	Fe(2)	Fe(3)	Fe(4)	Fe(5)
53K [001]	0.29061	0.08476	0.05967	0.05076	0.05301	0.04241
53K [100]	0.25549	0.06251	0.04822	0.04944	0.05068	0.04464
316K [001]	0.2855	0.0833	0.0574	0.0498	0.0524	0.0427
316K [100]	0.2572	0.0649	0.0478	0.0492	0.0505	0.0448
Temperature	Cr(1)	Cr(2)	Cr(3)	Cr(4)	Cr(5)	Cr(6)
53K [001]	0.00996	-0.00612	0.00935	-0.00746	0.0105	-0.01491
53K [100]	0.01182	-0.00607	0.00888	-0.00911	0.00931	-0.02182
316K [001]	0.0098	0.0062	0.0094	0.0075	0.0105	0.0150
316K [100]	0.0121	0.0062	0.0091	0.0090	0.0093	0.0211

## References

- [1] S. Ikeda, K. Miura, H. Yamamoto, K. Mizunuma, H. D. Gan, M. Endo, S. Kanai, J. Hayakawa, F. Matsukura, and H. Ohno, *Nat. Mater.* **9**, 721 (2010).
- [2] R. Shimabukuro, K. Nakamura, T. Akiyama, and T. Ito, *Physica E* **42**, 1014 (2010).
- [3] P.-J. Zermatten, G. Gaudin, G. Maris, M. Miron, A. Schuhl, C. Tiusan, F. Greullet, and M. Hehn, *Phys. Rev. B*, **78** 033301 (2008).
- [4] I. Rungger, O. Mryasov, and S. Sanvito, *Phys. Rev. B* **79**, 094414 (2009).
- [5] C.-G. Duan, J. P. Velev, R. F. Sabirianov, Z. Zhu, J. Chu, S. S. Jaswal, and E. Y. Tsymlal, *Phys. Rev. Lett.* **101**, 137201 (2008).
- [6] K. Nakamura, R. Shimabukuro, Yuji Fujiwara, T. Akiyama, T. Ito, and A. J. Freeman, *Phys. Rev. Lett.* **102**, 187201 (2009).
- [7] T. Nozaki, Y. Shiota, M. Shiraishi, T. Shinjo, and Y. Suzuki, *Appl. Phys. Lett.* **96**, 022506 (2010).
- [8] H. Ohno, *Nat. Mater.* **9**, 952 (2010).
- [9] M. Endo, S. Kanai, S. Ikeda, F. Matsukura, and H. Ohno, *Appl. Phys. Lett.* **96**, 212503 (2010).
- [10] T. Maruyama, Y. Shiota, T. Nozaki, K. Ohta, N. Toda, M. Mizuguchi, A. A. Tulapurkar, T. Shinjo, M. Shiraishi, S. Mizukami, Y. Ando, and Y. Suzuki, *Nat. Nanotechnol.* **4**, 158 (2009).
- [11] Y. Shiota, T. Nozaki, F. Bonell, S. Murakami, T. Shinjo, and Y. Suzuki, *Nat. Mater.* **11**, 39 (2012).

- 
- [12] Y. Hibino, T. Koyama, A. Obinata, T. Hirai, S. Ota, K. Miwa, S. Ono, F. Matsukura, H. Ohno, and D. Chiba, *Appl. Phys. Lett.* **109**, 082403 (2016).
- [13] Q. Xiang, Z. Wen, H. Sukegawa, S. Kasai, T. Seki, T. Kubota, K. Takanashi and S. Mitani, *J. Phys. D: Appl. Phys.* **50**, 40LT04 (2017).
- [14] N. Ikhsan, T. Kanagawa, I. Pardede, D. Yoshikawa and T. Oda, *The Sci. Rep. of Kanazawa Univ.* **62**, accepted (2018).
- [15] N. Ikhsan, I. Pardede, T. Kanagawa, D. Yoshikawa and T. Oda, *The Sci. Rep. of Kanazawa Univ.* **62**, accepted (2018).
- [16] T. Nozaki, A. Kozio-Rachwa, W. Skowroski, V. Zayets, Y. Shiota, S. Tamaru, H. Kubota, A. Fukushima, S. Yuasa, and Y. Suzuki: *Phys. Rev. Appl.* **5**, 044006 (2016).
- [17] J. W. Koo, H. Sukegawa, S. Kasai, Z. C. Wen, and S. Mitani, *J. Phys. D: Appl. Phys.* **47**, 322001 (2014).
- [18] J. Kanamori, "Anisotropy and Magnetostriction of Ferromagnetic and Antiferromagnetic Materials", in *Magnetism Volume 1* (H. Suhl and G. T. Rado, Academic Press, New York, 1963) Chap. 4, p. 127.
- [19] E. R. Callen and H. B. Callen, *J. Phys. Chem. Solids* **27**, 1271 (1966).
- [20] Y. Millev and M. Fähnle, *Phys. Rev. B*, **52**, 4336 (1995).
- [21] J.-U. Thiele, K. R. Coffey, M. F. Toney, J. A. Hedstrom, and A. J. Kellock, *J. Appl. Phys.* **91**, 6595 (2002).
- [22] S. Okamoto, N. Kikuchi, O. Kitakami, T. Miyazaki, Y. Shimada, and K. Fukamichi, *Phys. Rev. B* **66**, 24413 (2002).
- [23] O. N. Mryasov, U. Nowak, K. Y. Guslienko, and R. W. Chantrell, *Europhys. Lett.* **69** 805 (2005).

- [24] J. B. Staunton, S. Ostanin, S. S. A. Razee, B. L. Gyorffy, L. Szunyogh, B. Ginatempo, and E. Bruno, *Phys. Rev. Lett.* **93**, 257204 (2004).
- [25] I. A. Zhuravlev, V. P. Antropov, and K. D. Belashchenko, *Phys. Rev. Lett.* **115**, 217201 (2015).
- [26] J. G. Alzate, P. K. Amiri, G. Yu, P. Upadhyaya, J. A. Katine, J. Langer, *Appl. Phys. Lett.* **104**, 112410 (2014).
- [27] F. Bloch, *Z. Phys.* **61**, 10.1007 (1930).
- [28] Z. Wen, H. Sukegawa, T. Seki, T. Kubota, K. Takanashi, and S. Mitani, *Sci. Rep.* **7**, 45026 (2017).
- [29] U. Köbler, *J. Phys.: Condens. Mater* **14**, 8861 (2002).
- [30] P. S. Svendsen and U. von Barth. (1996). *Phys. Rev. B* **54**, 17402-17413.
- [31] J. P. Perdew and K. Burke. (1996). *Int. J. Quant. Chem.* **57**, 309-319.
- [32] D. Vanderbilt (1990). *Phys. Rev. B*, **41**, 7892.
- [33] N. D. Mermin, *Phys. Rev.* **137**, A1441 (1965).
- [34] H. Brooks, *Phys. Rev.* **58**, 909 (1940).
- [35] D. S. Wang, R. Wu, and A. J. Freeman, *Phys. Rev. B* **47**, 14932 (1993).
- [36] P. Bruno, “ Physical origins and the theoretical models of magnetic anisotropy ” in *Lecture Notes, IFF Ferienkurs Magnetismus von Festkörpern und Grenzflächen* 24 (P. H. Dedrichs, P. Grünberg and W. Zinn, Jülich). (1993) p.24.19.
- [37] T. Oda, M. Tsujikawa, *Surface Sci.* Vol. 29, No. 10, pp. 637-641, (2008).
- [38] <http://cphys.s.kanazawa-u.ac.jp/~oda/user-man-eng/>
- [39] H. J. Monkhorst and J. D. Pack, *Phys. Rev. B* **13**, 5188 (1976).

- 
- [40] M. Tsujikawa, A. Hosokawa, and T. Oda, *Phys. Rev. B* **77**, 054413 (2008).
- [41] N. Ikhsan, T. Kanagawa, I. Pardede, D. Yoshikawa, T. Oda, Submitted, (2018).
- [42] M. Weinert and J. W. Davenport, *Phys. Rev. B* **45**, 13709 (1992).
- [43] T. Oda, *J. Phys. Soc. Jpn*, **71**, 519 (2002).
- [44] G. H. O. Daalderop, P. J. Kelly, M. F. H. Schuurmans, and F. Jansen, *Phys. Rev. B* **41**, 11919 (1990).
- [45] M. Tsujikawa, A. Hosokawa and T. Oda, *Phys. Rev. B* **77**, 054413, (2008).
- [46] H. J. G. Draaisma and W. J. M. de Jonge, *J. Appl. Phys.* **64**, 3610 (1988).
- [47] T. Oda and M. Obata, *J. Phys. Soc. Jpn*, **87**, 064803 (2018).
- [48] T. Oda and A. Hosokawa, *Phys. Rev. B* **72**, 224428 (2005).
- [49] J. P. Perdew, J. A. Chevary, S. H. Vosko, K. A. Jackson, M. R. Pederson, D. J. Singh, and C. Fiolhais, *Phys. Rev. B* **46**, 6671 (1992).
- [50] J. W. Koo, H. Sukegawa, S. Kasai, Z. C. Wen, and S. Mitani, *J. Phys. D: Appl. Phys.* **47**, 322001 (2014).
- [51] D. Yoshikawa, M. Obata, and T. Oda, *JPS Conf. Proc.* **5**, 011012 (2015).
- [52] J. Zhang, Y. Wang, X.-G. Zhang, and X. F. Han, *Phys. Rev. B* **82**, 134449 (2010).
- [53] S. Cottenier, B. De Vries, J. Meersschant, and M. Rots, *J. Phys.: Condens. Matter* **14**, 3275 (2002).
- [54] M. Yu. Lavrentiev, R. Soulaïrol, Chu-Chun Fu, D. Nguyen-Manh, and S. L. Dudarev, *Phys. Rev. B* **84**, 144203 (2011).
- [55] L. Szunyogh, B. Ujfalussy, and P. Weinberger, *Phys. Rev. B* **51**, 9552 (1995).

- 
- [56] P. Bruno, Phys. Rev. B **39**, 865 (1989).
- [57] H. Hasegawa, Phys. Rev. B., **42**, 2368 (1990).
- [58] M. Ogura, H. Akai, and J. Kanamori, J. Phys. Soc. Jpn. **80**, 104711 (2011).
- [59] J. M. Ziman, *Principles of the theory of solids*, (Cambridge University Press, Cambridge, 1972), p. 343.
- [60] Y. Ando, T. Miyakoshi, M. Oogane, T. Miyazaki, H. Kubota, K. Ando, and S. Yuasa, Appl. Phys. Lett. **87**, 142502 (2005).
- [61] D.-S. Wang, R. Wu, and A. J. Freeman, Phys. Rev. B **48**, 15886 (1993).
- [62] A. Buruzs, P. Weinberger, L. Szunyogh, L. Udvardi, P. I. Chleboun, A. M. Fischer, and J. B. Staunton, Phys. Rev. B **76**, 064417 (2007).